The Astrophysical Journal, 908:17 (14pp), 2021 February 10 https://doi.org/10.3847/1538-4357/abd327

A Study of Gas Entropy Profiles of 47 Galaxy Clusters and Groups out to the Virial Radius

Zhenghao Zhu[1], Haiguang Xu[1,2], Dan Hu[1], Chenxi Shan[1], Yongkai Zhu[1], Shida Fan[1], Yuanyuan Zhao[1], Liyi Gu[3,4], and Xiang-Ping Wu[5]
[1] School of Physics and Astronomy, Shanghai Jiao Tong University, 800 Dongchuan Road, Minhang, Shanghai 200240, People's Republic of China
hgxu@sjtu.edu.cn
[2] IFSA Collaborative Innovation Center, Shanghai Jiao Tong University, 800 Dongchuan Road, Shanghai 200240, People's Republic of China
[3] RIKEN High Energy Astrophysics Laboratory, 2-1 Hirosawa, Wako, Saitama 351-0198, Japan
[4] SRON Netherlands Institute for Space Research, Sorbonnelaan 2, 3584 CA Utrecht, The Netherlands
[5] National Astronomical Observatories, Chinese Academy of Sciences, 20A Datun Road, Beijing 100012, People's Republic of China
Received 2020 July 10; revised 2020 December 4; accepted 2020 December 10; published 2021 February 9

Abstract

Some observations, such as those presented in Walker et al., show that the observed entropy profiles of the intracluster medium (ICM) deviate from the power-law prediction of adiabatic simulations. This implies that nongravitational processes, which are absent in the simulations, may be important in the evolution of the ICM, and by quantifying the deviation, we may be able to estimate the feedback energy in the ICM and use it as a probe of the nongravitational processes. To address this issue, we calculate the ICM entropy profiles in a sample of 47 galaxy clusters and groups, which have been observed out to at least $\sim r_{500}$ with Chandra, XMM-Newton, and/or Suzaku, by constructing a physical model to incorporate the effects of both gravity and nongravitational processes to fit the observed gas temperature and surface brightness profiles via Bayesian statistics. After carefully evaluating the effects of systematic errors, we find that the gas entropy profiles derived with best-fit results of our model are consistent with the simulation-predicted power-law profile near the virial radius, while the flattened profiles reported previously can be explained by introducing the gas clumping effect, the existence of which is confirmed in 19 luminous targets in our sample. We calculate the total feedback energy per particle and find that it decreases from $\sim$10 keV at the center to about zero at $\sim 0.35 r_{200}$ and is consistent with zero outside $\sim 0.35 r_{200}$, implying an upper limit of the feedback efficiency of $\sim$0.02 for the supermassive black holes hosted in the brightest cluster galaxies.

Unified Astronomy Thesaurus concepts: Galaxy clusters (584); Intracluster medium (858); X-ray sources (1822)

1. Introduction

In terms of the hierarchical structure formation scenario (Press & Schechter 1974), the primordial density fluctuations grow into galaxies, which evolve into protoclusters and then more massive systems via accretion of surrounding materials and mergers with other clusters (Voit et al. 2005; Springel et al. 2018). Although the whole process is expected to be dominated by gravity, the nongravitational processes—including the feedback of active galactic nuclei (AGNs), which has become a very active topic in the recent decade (see Fabian 2012 for a review), radiation of the intracluster medium (ICM), conduction within the ICM, a possible preheating at the early stage of the cluster formation, etc.—may also have chances to play important roles (e.g., Vazza 2011). In fact, considerable or relatively minor heat exchanging happens in all these processes. Therefore, the thermodynamical properties of the ICM change accordingly, depending on the timescales and space scales considered (Iqbal et al. 2017). For example, AGNs can break the hydrostatic equilibrium via heating the ICM in the core regions with the energetic outflows (Vazza et al. 2013), and the radiative cooling of the gas tends to produce a cooler but brighter cluster core, which often appears as a so-called cool core (Hudson et al. 2010). Thus, the theoretically predicted mass–luminosity and mass–temperature relations are broken (Kaiser 1986). Therefore, the details of nongravitational processes must be carefully treated while studying the structures of the ICM and their evolutionary histories (e.g., Voit et al. 2002; Planelles et al. 2013; Lovell et al. 2018).

Among various gas properties the entropy K, usually defined as $T \times n_e^{-2/3}$ in astrophysical literature (Voit et al. 2005), where T and n_e are the temperature and the electron density of the ICM, respectively, is one of the probes most sensitive to the nongravitational processes, because it is the logarithm of the entropy S in thermodynamics, which is directly related to the net change of heat energy dQ via $dQ = TdS$ (see Section 4 for detail). By comparing the observed gas entropy profiles with those predicted under the assumption of pure gravity, we may be able to evaluate the contribution of nongravitational processes and estimate the corresponding net heat supply in the ICM (e.g., Chaudhuri et al. 2012; Iqbal et al. 2017).

Results of nonradiative (i.e., no feedback or cooling is considered) hydrodynamical simulations show that outside the cluster core the ICM entropy profile scales as $\propto r^{1.1}$ (e.g., Voit et al. 2002, 2005). Studies such as Su et al. (2015) and Tchernin et al. (2016) do show that the observed gas entropy profiles are consistent with the power-law profile out to r_{200}. On the other hand, however, studies based on many X-ray observations performed with Chandra, XMM-Newton, and Suzaku (e.g., Bautz et al. 2009; Kawaharada et al. 2010; Akamatsu et al. 2011; Ichikawa et al. 2013; Ghirardini et al. 2019) indicate that near the virial radius the observed gas entropy profiles differ more or less from the power-law prediction. Walker et al. (2012a, hereafter W12a) studied a sample of 11 clusters ($z < 0.25$) probed out to $\sim r_{200}$ and found that most of the observed entropy profiles follow a universal shape that starts to flatten at around r_{500}.[6] In order to explain these confusing inconsistent results, Ghirardini et al. (2019) have

[6] r_δ is the radius within which the mean mass density is δ times the critical density of the local universe.

attempted to attribute the flattening of the gas entropy profiles detected in their sample of 12 clusters to the fact that the gas clumping effect is not taken into account in modeling the X-ray surface brightness. In fact, if the actual gas distribution is clumpy, the assumption of uniform distribution of gas density in the model is found to result in a higher average gas density and then a lower entropy (e.g., Roncarelli et al. 2006; Vazza 2011), causing the entropy profile to be flatter than the power-law prediction. Besides the clumping effect, the dynamical nonequilibrium of ICM caused by bulk motions or turbulence (Okabe et al. 2014; Khatri & Gaspari 2016), the unbalance thermodynamical state between the electron or ion populations (Hoshino et al. 2010), and the adiabatic expansion caused by the weakening of the accretion processes in a relaxed cluster (Lapi et al. 2010) have also been proposed to explain the flattening of the entropy profiles near the virial radius. The reason for the inconsistency remains controversial up to now.

In order to solve this interesting problem, a large sample analyzed with a high signal-to-noise ratio (S/N) and a sufficiently good spatial resolution is apparently needed. In this work we built a sample containing 47 galaxy clusters and groups that have been observed out to at least $\sim r_{500}$ and applied a revised thermodynamical ICM model (RTI model), which is improved from the analytic model presented in Zhu et al. (2016, hereafter Z16), to describe the observed gas temperature, surface brightness, and total mass distributions. By using the best-fit parameters to investigate the gas entropy distributions, which are evaluated with the uncertainties caused by different systematic effects primarily in instrument calibrations and in the modeling of the plasma emission, we conclude that the gas entropy profiles near the virial radius are consistent with the power-law prediction within the 68% confidence range. We also calculate the feedback energy using the derived gas entropy profiles and obtain a moderate feedback efficiency of ∼0.02 for the supermassive black holes (SMBHs) hosted in the brightest cluster galaxies (BCGs).

This paper is organized as follows. In Section 2 we describe the sample selection criteria. In Section 3 we describe the data analysis procedure for Chandra observations, which covers the $\sim 0.3 r_{500}$ regions for all sample targets. Meanwhile, we search in the literature for works based on Chandra, XMM-Newton, or Suzaku observations that cover out to at least r_{500}, and we quote the observed gas temperature and X-ray surface brightness presented therein. These profiles, together with those obtained in our Chandra analysis for the inner $0.3 r_{500}$, will be fed into our model as observational constraints. In Section 4 we describe our model and use it to fit the observed gas temperature and X-ray surface brightness profiles prepared in Section 3, and we use the best-fit results to calculate the gas entropy profiles. Our results are discussed in Section 5 and summarized in Section 6. Throughout this work we adopt a flat ΛCDM cosmology with $\Omega_m = 0.27$, $\Omega_\lambda = 0.73$, and the Hubble constant $H_0 = 71$ km s^{-1} Mpc^{-1}. Unless otherwise stated, we use the solar abundance standards of Grevesse & Sauval (1998) and quote errors at the 68% confidence level.

2. Sample Construction

In order to characterize the entropy profiles accurately and precisely with sufficient spatial resolution, we construct our sample from the clusters and groups satisfying the following criteria: (1) The X-ray surface brightness and gas temperature of the target should have been measured out to at least $\sim r_{500}$ with Chandra, XMM-Newton, or Suzaku in previous studies (Table 1) with available gas temperature and X-ray surface brightness data that can be quoted and used in the RTI model fitting. (2) Because the extended, irregular, and energy-dependent point-spread functions (PSFs) of XMM-Newton and Suzaku (e.g., Snowden et al. 2008; Sugizaki et al. 2009) have a nonnegligible effect on the analysis of the observed data, especially in central regions, we download and analyze the corresponding Chandra data for the inner $0.3 r_{500}$ to better constrain the RTI model fitting. (3) The S/N of the data should be at least 1.5 at $\sim r_{500}$. (4) The target should exhibit a relatively regular appearance and have no remarkable substructure to guarantee that the assumption of the spherical symmetry used in Section 4 is valid. As a result, we find 47 clusters and groups in the literature that satisfy the above conditions (Table 1), the redshifts and averaged temperatures of which span the ranges 0.0036–0.63 and 1.7–11.8 keV, respectively.

3. Chandra Data Analysis

3.1. Data Preparation

The Chandra data are reduced by following the method described in Z16. In brief, for each cluster or group we start from Chandra ACIS level 1 event files and use the CIAO[7] script (version 4.11 with calibration database CALDB, v4.8.2) `chandra_repro` to generate level 2 event files. After identifying and excluding point sources using the CIAO tool `celldetect`, the results of which have been cross-checked via visual examination, we examine the light curves extracted in 0.5–12.0 keV from the source-free regions near the CCD edges and filter the time intervals during which the count rate deviates from the mean value by 20%.

3.2. Data Analysis

In this subsection we calculate the X-ray surface brightness and gas temperature profiles to be used in the RTI model fitting (Section 4) by fitting the Chandra ACIS data. We first extract the surface brightness profiles in 0.7–7.0 keV from a set of concentric annuli that are centered at the X-ray centroid and use the exposure maps generated with the CIAO tool `flux_image` to correct for the vignetting effect and exposure fluctuations. Then, we derive the gas temperature profiles by analyzing the spectra extracted in 0.7–7 keV from another set of annuli, which are also centered at the X-ray centroid but are wider to include a minimum of 2500 photon counts per annulus. The extracted spectra are corrected using the redistribution matrix files and ancillary response files generated with the CIAO script `specextract` after subtracting the backgrounds, which are created by following the method given in Z16. To fit the spectra, we apply the multiplication of XSPEC models (1) `PROJCT` to correct for the deprojection effect; (2) two `APEC` components (one for the thermal emission of the optically thin ICM, and the other for the possible cool phase gas that is often observed in the central region; e.g., Makishima et al. 2001; the abundances of both `APEC` components are set free unless either or both of them cannot be well constrained; in this case we fix the abundance of the corresponding component to 0.3 solar; e.g., Panagoulia et al. 2014); and (3) `WABS` to model the photoelectric absorption, which is fixed to the Galactic value (Kalberla et al. 2005). If the *F*-test shows that the two-phase fitting is not

[7] Chandra Interactive Analysis of Observations; please refer to https://cxc.harvard.edu/ciao/.

Table 1
The Sample

Name	Chandra ObsID[a]	Detector	R.A.[b]	Decl.[b]	Redshift[c]	References[d]
1E 1455.0+2232	4192	ACIS-I	14:57:15.1	+22:20:34	0.258	Snowden et al. (2008)[2]
A1068	1652	ACIS-S	10:40:43.9	+39:56:53	0.147	Snowden et al. (2008)[2]
A1246	11770	ACIS-I	11:23:50.0	+21:25:31	0.190	Sato et al. (2014)[3]
A133	9897	ACIS-I	01:02:42.1	−21:52:25	0.057	Morandi & Cui (2014)[1]
A13	4945	ACIS-S	00:13:38.3	−19:30:08	0.103	Snowden et al. (2008)[2]
A1413	5003	ACIS-I	11:55:18.9	+23:24:31	0.143	Hoshino et al. (2010)[3]
A1689	6930	ACIS-I	13:11:29.5	−01:20:17	0.183	Kawaharada et al. (2010)[3]
A1775	13510	ACIS-S	13:41:53.8	+26:22:19	0.075	Snowden et al. (2008)[2]
A1795	10898	ACIS-I	13:48:53.0	+26:35:44	0.062	Bautz et al. (2009)[3]
A1835	6880	ACIS-I	14:01:02.3	+02:52:48	0.253	Ichikawa et al. (2013)[3]
A2029	4977	ACIS-S	15:10:55.0	+05:43:12	0.077	Walker et al. (2012c)[3]
A209	3579	ACIS-I	01:31:53.0	−13:36:34	0.212	Snowden et al. (2008)[2]
A2142	5005	ACIS-I	15:58:20.6	+27:13:37	0.091	Tchernin et al. (2016)[2]
A2163	1653	ACIS-I	16:15:34.1	−06:07:26	0.202	Snowden et al. (2008)[2]
A2199	10748	ACIS-I	16:28:38.0	+39:32:55	0.030	Sato et al. (2014)[3]
A2204	7940	ACIS-I	16:32:46.5	+05:34:14	0.152	Reiprich et al. (2009)[3]
A2255	894	ACIS-I	17:12:31.0	+64:05:33	0.081	Akamatsu et al. (2017)[3]
A2319	3231	ACIS-I	19:21:08.8	+43:57:30	0.056	Ghirardini et al. (2019)[2]
A2597	7329	ACIS-S	23:25:20.0	−12:07:38	0.080	Snowden et al. (2008)[2]
A2667	2214	ACIS-S	23:51:40.7	−26:05:01	0.221	Snowden et al. (2008)[2]
A3158	3712	ACIS-I	03:42:53.9	−53:38:07	0.060	Ghirardini et al. (2019)[2]
A3266	899	ACIS-I	04:31:24.1	−61:26:38	0.059	Ghirardini et al. (2019)[2]
A383	2320	ACIS-I	02:48:02.0	−03:32:15	0.187	Snowden et al. (2008)[2]
A478	1669	ACIS-S	04:13:25.6	+10:28:01	0.088	Pointecouteau et al. (2004)[2]
A644	2211	ACIS-I	08:17:24.5	−07:30:46	0.070	Ghirardini et al. (2019)[2]
A68	3250	ACIS-I	00:37:05.3	+09:09:11	0.248	Snowden et al. (2008)[2]
A773	5006	ACIS-I	09:17:59.4	+51:42:23	0.216	Snowden et al. (2008)[2]
AS1101	11758	ACIS-I	23:13:58.6	−42:44:02	0.056	Snowden et al. (2008)[2]
Centaurus Cluster	4955	ACIS-S	12:48:47.9	−41:18:28	0.011	Walker et al. (2013)[3]
Cl 0016+16	520	ACIS-I	00:18:33.8	+16:26:17	0.541	Kotov & Vikhlinin (2005)[2]
Cl 0024+17	929	ACIS-S	00:26:35.7	+17:09:46	0.390	Kotov & Vikhlinin (2005)[2]
Coma Cluster	13993	ACIS-I	12:59:48.7	+27:58:50	0.023	Simionescu et al. (2013)[3]
ESO 306-G 017 group	3188	ACIS-I	05:40:06.3	−40:50:32	0.036	Su et al. (2013)[3]
HydraA Cluster	4970	ACIS-S	09:18:06.5	−12:05:36	0.054	Sato et al. (2012)[3]
Perseus Cluster	11714	ACIS-I	03:19:47.2	+41:30:47	0.018	Urban et al. (2014)[3]
PKS 0745-191 Cluster	6103	ACIS-I	07:47:32.4	−19:17:32	0.103	Walker et al. (2012b)[3]
RXC J0605.8−3518	15315	ACIS-I	06:05:52.8	−35:18:02	0.137	Miller et al. (2012)[3]
RXC J1825.3+3026	13381	ACIS-I	18:25:24.7	+30:26:31	0.065	Ghirardini et al. (2019)[2]
RXC J2234.5−3744	15303	ACIS-I	22:34:31.0	−37:44:06	0.154	Snowden et al. (2008)[2]
RX J1120.1+4318	5771	ACIS-I	11:20:07.4	+43:18:07	0.600	Kotov & Vikhlinin (2005)[2]
RX J1159.8+5531	4964	ACIS-S	11:59:51.1	+55:31:56	0.081	Su et al. (2015)[1]
RX J1334.3+5030	5772	ACIS-I	13:34:20.4	+50:31:05	0.620	Kotov & Vikhlinin (2005)[2]
RX J1347.5−1145	3592	ACIS-I	13:47:30.6	−11:45:10	0.451	Snowden et al. (2008)[2]
UGC 03957 Cluster	8265	ACIS-I	07:40:58.3	+55:25:37	0.034	Thölken et al. (2016)[3]
Virgo Cluster	7212	ACIS-I	12:30:47.3	+12:20:13	0.0036	Simionescu et al. (2017)[3]
ZwCl 1215.1+0400	4184	ACIS-I	12:17:40.6	+03:39:45	0.075	Ghirardini et al. (2019)[2]
ZwCl 3146	909	ACIS-I	10:23:39.0	+04:11:14	0.282	Snowden et al. (2008)[2]

Notes.
[a] The observation with the longest exposure time is chosen when multiple observations exist. Observations performed with ACIS-I are preferred if the target has been observed with both ACIS-I and ACIS-S.
[b] Right ascensions and declinations are in J2000.0.
[c] Redshifts are taken from NASA Extragalactic Database.
[d] The superscripts 1, 2, and 3 in this column represent that the Chandra, XMM-Newton, and Suzaku data are quoted from the literature, respectively.

significantly better (p-value > 0.05) than the case when the cool phase is ignored, we choose the single-phase gas model.

4. RTI Model Analysis of the Sample

4.1. RTI Model Description

In this section we introduce the RTI model used to fit the observed gas temperature and surface brightness profiles, which is an improved version of the model we presented in Z16. Similar to what we have done in Z16, for a given test element that contains n^* gas particles we assume that the current total energy contained in the gas is supplied by (1) the energy injected through gravitational collapse ($\Delta E_{\rm G}(r)$); (2) the net heat obtained in its thermal history ($\Delta E_{\rm heating}(r)$) via feedback processes, radiative cooling, thermal conduction, etc.; and (3) the work done by surrounding particles through volume

change ($\Delta E_{\rm work}(r)$). Since the current gas thermal energy occupies only part of $\Delta E_{\rm G}(r)+\Delta E_{\rm heating}(r)+\Delta E_{\rm work}(r)$ (the rest is stored in turbulence or bulk motions), it can be found that (see Equations (6) and (13) in Z16) the gas temperature profile should have the form

$$T(r)=\frac{2\eta(r)(E_0+\Delta E_{\rm G}(r)+\Delta E_{\rm work}(r)+\Delta E_{\rm heating}(r))}{3n^*k_{\rm B}}, \tag{1}$$

where $\eta(r)$ is the fraction of the thermal pressure to the total pressure, E_0 ($\sim$0) represents the initial energy of the gas element, and $k_{\rm B}$ is the Boltzmann constant.

Energy injected through gravitational collapse: To calculate $\Delta E_{\rm G}(r)$, we assume a generalized NFW profile (Navarro et al. 1997) to describe the total gravitational mass distribution, which is

$$\rho(r)=\frac{\rho_0}{(r/r_s)^{\delta_1}(1+r/r_s)^{\delta_2-\delta_1}}, \tag{2}$$

where r_s is the scale radius, ρ_0 is the central density, and δ_1/δ_2 represents the inner/outer slope. Thus, the corresponding total energy input via gravitational collapse (see Equation (7) in Z16) can be calculated as

$$\Delta E_{\rm G}(r)=\frac{G\int_0^r\rho(x)4\pi x^2m^*dx}{r}+\int_r^\infty\frac{G\rho(x)4\pi x^2m^*dx}{x}, \tag{3}$$

where G is the gravitational constant and $m^*=n^*\mu m_{\rm p}$ is the mass of the test gas element (where $m_{\rm p}$ is the proton mass and $\mu=0.61$ is the mean molecular weight).

Net heat supply: The net heat supply $\Delta E_{\rm heating}(r)$ is estimated using the thermodynamic relation $dQ=TdS$, where S is the thermodynamical entropy. Here we adopt the Boltzmann entropy for the ideal gas, one of the most frequently used thermodynamical entropies (they differ from each other by only a constant), to calculate dQ (Kardar 2007), which is

$$S=n^*k_{\rm B}(1.5+1.5\ln(2\pi m^*k_{\rm B}T)-\ln(n^*/V^*)), \tag{4}$$

where V^* is the volume of the test gas element. The change of entropy between any states 1 and 2 is then written as

$$S_2-S_1=n^*k_{\rm B}\ln\left(\frac{T_2^{1.5}V_2^*}{T_1^{1.5}V_1^*}\right), \tag{5}$$

or, considering that the conventional definition of astrophysical entropy is $K=Tn_{\rm e}^{-2/3}$,

$$S_2-S_1=1.5n^*k_{\rm B}\ln(K_2/K_1). \tag{6}$$

Taking the limit state 2 $\rightarrow$ state 1, we have $dS=1.5n^*k_{\rm B}dK/K$. Therefore, by substituting dS into the expression $dQ=TdS$, the net heat supply in the nongravitational processes becomes

$$\Delta E_{\rm heating}(r)=\int dQ(r)=\int_{K_{\rm sim}}^{K_{\rm obs}}1.5n^*k_{\rm B}T(r)dK/K(r), \tag{7}$$

where $K_{\rm sim}$ is the simulated entropy of the gas element if only the gravitational effect is considered (Voit et al. 2005), and $K_{\rm obs}$ is the observed entropy. We estimate the integration in Equation (7) using the method of Chaudhuri et al. (2012),

$$\Delta E_{\rm heating}(r)=C_hn^*k_{\rm B}T(r)(K_{\rm obs}(r)-K_{\rm sim}(r))/K_{\rm obs}(r), \tag{8}$$

where C_h is the scaling factor. Voit et al. (2005) showed that when only the gravitational effect is considered (see their Equation (5)),

$$K_{\rm sim}(r)=K_0+A_0\times\frac{r}{1\ {\rm kpc}}^{\gamma_0}, \tag{9}$$

where K_0 is the central entropy, A_0 is the normalization, and γ_0 is the slope of the entropy profile. To express the observed entropy $K_{\rm obs}(r)$, which will be derived later by fitting the observed gas temperature and X-ray surface brightness with the model described here, we adopt the electron density profile $n_{\rm e}(r)$ following Patej & Loeb (2015),

$$n_{\rm e}(r)=\frac{\Gamma f_g}{\mu_{\rm e}m_{\rm p}}\left(\frac{r}{r_{\rm shock}}\right)^{3\Gamma-3}\rho\left(r_{\rm shock}\left[\frac{r}{r_{\rm shock}}\right]^{\Gamma}\right), \tag{10}$$

where $r_{\rm shock}$ is the radius where virial shock happens, $\mu_{\rm e}=1.18$ is the mean molecular weight per electron, Γ is the ratio used to measure the gas density jump at $r_{\rm shock}$, f_g is the gas fraction within $r_{\rm shock}$, and ρ is the total mass density (Equation (2)).

Work done by surrounding particles: We calculate $\Delta E_{\rm work}$ by assuming that the gas element has experienced a polytropic process during the gravitational collapse. Thus, we calculate $\Delta E_{\rm work}(r)$ (see Equation (9) in Z16) as

$$\Delta E_{\rm work}(r)=\frac{\nu_{\rm mol}^*\mathcal{R}}{n-1}\left(T(r)-\frac{2C_w\Delta E_{\rm G}(r)}{3n^*k_{\rm B}}\right), \tag{11}$$

where n is the polytropic index and C_w is the fraction of the gravitational energy that has been transformed into the thermal energy before the polytropic process, both of which are to be determined in the fitting, and ${\nu_{\rm mol}}^*=n^*/N_{\rm A}$ is the mole number ($N_{\rm A}$ is the Avogadro constant).

Model-predicted gas temperature and X-ray surface brightness: Following Nelson et al. (2014), we write the thermal pressure fraction $\eta(r)$ in Equation (1) as

$$\eta(r)=\frac{P_{\rm thermal}}{P_{\rm tot}}=A\left(1+\exp\left[-\left(\frac{r/r_{200}}{B}\right)^{\gamma}\right]\right), \tag{12}$$

where $P_{\rm thermal}$ and $P_{\rm tot}$ are the thermal and total pressure, respectively (A, B, and γ are empirical parameters calculated in Nelson et al. 2014). Note that when $\eta(r)=1$ (cases 3, 4, and 5 in Section 5.2), the nonthermal pressure vanished. Now, the model-predicted gas temperature distribution can be obtained by substituting Equations (3), (8), (11), and (12) into Equation (1). To write it in a simple analytical form, we introduce $e_{\rm gen}(r)\equiv\Delta E_{\rm G}(r)/\Delta E_{\rm G,ref}(r)$, where the reference term $\Delta E_{\rm G,ref}(r)$ is calculated using Equation (3) by setting $\delta_1\equiv1$ and $\delta_2\equiv3$ (when δ_1 and δ_2 are not integers, $\Delta E_{\rm G}(r)$ has no analytical expression). Thus,

$$T(r)=\frac{T_0+e_{\rm gen}(r)(1-C_wN_3)N_1\rho_0r_s^3\ln((r_s+r)/r_s)/r-K_{\rm sim}(r)/n_{\rm e}^{-2/3}(r)}{1/\eta(r)-N_3-N_2}, \tag{13}$$

where $T_0=2E_0/3k_{\rm B}$ is assumed to be $\simeq$0, $N_1=8\pi G\mu m_{\rm p}/3$ is a fixed combination of physical constants, $N_2=2C_h/3$, and

Table 2
Priors of Model Parameters

Parameter	Mean[a]	Standard Deviation[a]	Min	Max	References
ρ_0 ($M_\odot$ kpc^{-3})	N/A	N/A	0	10^7	N/A
r_s (Mpc)	N/A	N/A	0	1	N/A
δ_1	1.0	0.5	0	2	Navarro et al. (1997)
δ_2	3.0	0.5	2	10	Navarro et al. (1997)
A_0 (keV cm^2)	0.5	1.0	0	5	Voit et al. (2005)
γ_0	1.1	0.2	0	3	Voit et al. (2005)
K_0 (keV cm^2)	N/A	N/A	0	1000	Voit et al. (2005)
Γ	1.3	0.5	1.0	5.0	Patej & Loeb (2015)
f_g	0.13	0.03	0	0.3	Patej & Loeb (2015)
$r_{\rm shock}$ (Mpc)	N/A	N/A	2	10	Patej & Loeb (2015)
A	0.45	0.2	0	0.5	Nelson et al. (2014)
B	1.4	0.7	0	N/A	Nelson et al. (2014)
γ	1.6	0.8	0	N/A	Nelson et al. (2014)
N_2	1.0	0.2	0	5	Chaudhuri et al. (2012)
N_3	N/A	N/A	0	10	N/A
C_w	N/A	N/A	0	1	N/A
c_1	−3.7	1.0	−10	10	Vazza et al. (2013)
c_2	3.7	1.0	−10	10	Vazza et al. (2013)
c_3	N/A	N/A	0	5	Vazza et al. (2013)
c_4	N/A	N/A	0	0.1	Vazza et al. (2013)
c_5	N/A	N/A	0	0.1	Vazza et al. (2013)

Note.
[a] When the mean and standard deviation for a model parameter are not available, we adopt a uniform prior (i.e., no prior is assumed). Otherwise, a Gaussian distribution is assigned (e.g., Andreon & Hurn 2012).

$N_3 = 2/(3(n-1))$. The three-dimensional temperature profiles calculated using Equation (13) or the corresponding two-dimensional profiles obtained by projecting the three-dimensional profiles using the method of Mazzotta et al. (2004), i.e.,

$$T_{\rm 2d}(R) = \frac{\int_R^\infty n_{\rm e}^2(r) T^{0.25}(r) dr}{\int_R^\infty n_{\rm e}^2(r) T^{-0.75}(r) dr}, \quad (14)$$

can be directly compared with the observed temperatures.

The model-predicted X-ray surface brightness profile is

$$S_{\rm model}(R) = \int_R^\infty C(r)\Lambda(T, Z)\bar{n}_{\rm e}\bar{n}_{\rm p}(r)\frac{2rdr}{\sqrt{r^2 - R^2}} + S_{\rm bkg}, \quad (15)$$

where $n_{\rm p}$ is the proton number density ($\simeq n_{\rm e}/1.2$ for a fully ionized ICM; Cavagnolo et al. 2009), $\Lambda(T, Z)$ is the cooling function calculated using the temperature derived from Equation (13) and the abundance given in the references listed in Table 1, $S_{\rm bkg}$ is the diffuse X-ray background, and $C(r)$ is the clumping factor to characterize the level of inhomogeneities in the ICM. In the literature $C(r)$ is usually defined as

$$C(r) \equiv \frac{\langle \rho_{\rm gas}^2(r) \rangle}{\langle \rho_{\rm gas}(r) \rangle^2}, \quad (16)$$

where $\langle \cdot \rangle$ denotes the average operation inside a spherical shell, so that $C(r) = 1$ (cases 2–5 in Section 5.2) when the clumping effect does not exist. In the high-resolution cosmological simulations of Vazza et al. (2013), where the effects of AGN feedback and gas cooling were both considered, the radial variation of the clumping factor was found to obey the following empirical relation:

$$C(r)^{0.5} = (1 + r/r_{200})^{c_1}\exp(c_2 r/r_{200}) + c_3\exp\left[\frac{-(r/r_{200} - c_4)^2}{c_5}\right], \quad (17)$$

where c_1–c_5 are free parameters to be determined in the model fitting.

4.2. Markov Chain Monte Carlo Sampling and Results of RTI Model Fitting

Similar to Z16, we employ the Bayesian approach (see Andreon & Hurn 2012 for a review), which can be used to quantify the intrinsic scatters and uncertainties of known model parameters (i.e., all parameters listed in Table 2), and meanwhile incorporate observation errors (i.e., both statistic and systematic errors of observed temperature and surface brightness; a more detailed discussion on systematic errors is presented in Section 5.1) in the model fittings. In the Bayesian approach, the Markov Chain Monte Carlo (MCMC) algorithm is often adopted since it is possible to use it to perform straightforward fittings to a complicated model with huge numerical calculations at a moderate convergence speed. After the convergence is achieved, the MCMC algorithm iteratively generates a large number of samples from the true joint distribution of the model parameters (Trotta 2017) that can be used to estimate the possibility distributions of all model parameters (functions of these parameters). In this work we employ the Metropolis–Hastings MCMC (Hastings 1970) that is implemented by the software PyMC[8] to obtain the best-fit model parameters by maximizing the posterior (i.e., the possibility of the fitted parameters for given observed data

[8] https://github.com/pymc-devs/pymc

sets), which is calculated by multiplying the prior (i.e., our knowledge of the model parameters obtained before the fittings are carried out; see Table 2) and the likelihood function L (i.e., the possibility of the observed data; see Andreon & Hurn 2012),

$$L = \prod_i \frac{1}{\sqrt{2\pi\sigma_{x,i}^2}} \exp\left[-\frac{(x_{i,\rm obs} - x_{i,\rm model})^2}{2\sigma_{x,i}^2}\right], \quad (18)$$

where $x_{i,\rm obs}$ represents the observed variables, including gas temperature and X-ray surface brightness, as well as the total gravitating mass; $\sigma_{x,i}$ represents the standard deviation of the corresponding $x_{i,\rm obs}$; and $x_{i,\rm model}$ represents the corresponding model-predicted value. We have performed a split test (Morandi & Sun 2016) to ensure the convergence of the MCMC chains, i.e., for each sample member the MCMC chain is split into two series after the burn-in (i.e., the first part of iterations in the MCMC chain before it converges) is removed, and the model parameters derived with the two split chains are compared with each other to make sure their 68% confidence ranges overlap each other. The number of MCMC iterations is set to 5×10^5, and the first 2×10^5 iterations are regarded as burn-in to ensure the convergence.

In Table 3 we list best-fit results, together with the goodness of fit described with the model efficiency $R_{\rm eff}$ (see Z16 and references therein),

$$R_{\rm eff} = \frac{1}{N_{\rm bin}} \sum_{i=1}^{N_{\rm bin}} R_{{\rm eff},i}, \quad (19)$$

in which

$$R_{{\rm eff},i} = 1 - \frac{\sum_{n=1}^{N_{\rm sample}} (X_{i,n,\rm sample} - \bar{X}_{i,\rm obs})^2}{\sum_{n=1}^{N_{\rm sample}} (X_{i,n,\rm obs} - \bar{X}_{i,\rm obs})^2}, \quad (20)$$

where $N_{\rm bin}$ is the total bin number of the observed quantities (i.e., temperature, surface brightness, and total mass), $N_{\rm sample}$ is the number of MCMC iterations, and $X_{\rm sample}$ and $X_{\rm obs}$ are used to represent any sampled and observed physical quantities, respectively. We find that a reasonable fit ($R_{\rm eff} \gtrsim 0$; if the fitting is based on the χ-square statistic, $R_{\rm eff} \gtrsim 0$ implies $\chi_\nu^2 \lesssim 1$; see also Engeland & Gottschalk 2002) has been obtained for all targets in the sample. Then, we calculate the entropy profiles using the best-fit gas densities and temperature profiles and plot them in Figure 1, with the simulation-predicted entropy profiles (Voit et al. 2005), which are scaled by r_{200} and $K(r_{500})$. It showed that no apparent flattening of the gas entropy profile can be confirmed near $\sim r_{200}$.

To quantify the statistical significance of the result that best-fit entropy profiles generally converge asymptotically to the baseline profile near the virial radius, we perform the χ^2 fitting to the observed entropy profile ($K_{\rm obs}$) with the power-law model (Voit et al. 2005), i.e.,

$$\frac{K_{\rm obs}}{K_{200}} = K_1 + A_1 \times \left(\frac{r}{r_{200}}\right)^{\gamma_1}, \quad (21)$$

where γ_1 is the slope of the entropy profile, A_1 is the normalization, and K_1 is the scaled central entropy. In order to compare the best-fit parameters directly to the baseline prediction, we define the scaling factor K_{200} following Voit et al. (2005), i.e.,

$$K_{200} = 362\ {\rm keV\ cm^2} \frac{T_{200}}{1\ {\rm keV}} \times \left[\frac{H(z)}{H_0}\right]^{-4/3} \left(\frac{\Omega_m}{0.3}\right)^{-4/3}, \quad (22)$$

where

$$T_{200} \equiv \frac{GM_{200}\mu m_{\rm p}}{2r_{200}}. \quad (23)$$

We find that for all sample members the reduced χ^2 is less than or approximately equal to 1, which implies that the power-law model is sufficient to describe the entropy profile. In Figure 2 we plot the best-fit coefficients of the power-law model and their uncertainties for each sample member as a function of M_{500}. We find that A_1 and γ_1 generally fall in the predicted range of the baseline simulations (e.g., Tozzi & Norman 2001; Voit et al. 2005). K_1, on the other hand, diverts from the baseline prediction (see Figure 5 of Voit et al. 2005), implying that the feedback processes and the radiative cooling significantly affect the thermal properties of the ICMs in the core regions of galaxy clusters and groups.

5. Discussions

5.1. Impact of Systematic Errors

The results obtained with our model may be biased by systematic errors, primarily including the uncertainties in calibrating instruments and the simplifications made in the calculations (e.g., Cavagnolo et al. 2009; Buote et al. 2016). In order to validate our results in the following subsection, we will focus on eight error sources that exist in measuring gas temperature and X-ray surface brightness; actually the errors caused by these sources have been taken into account in the fittings in Section 4.2.

5.1.1. Systematic Errors in Measuring Gas Temperature

Instrument calibration: Primarily due to the energy-dependent difference in effective areas between the X-ray instruments on board Chandra, XMM-Newton, and Suzaku, even after careful calibration the gas temperatures measured with these instruments always exhibit differences, the level of which may depend on the temperature of the target. As pointed out in Kettula et al. (2013) and Schellenberger et al. (2015), the difference of the temperatures measured with Chandra and XMM-Newton can be about 7%, 16%, and 23% for targets with averaged temperature 2, 5, and 10 keV, respectively, while the difference between the XMM-Newton and Suzaku measurements is about ∼5%, which is less temperature dependent. In this work we evaluate the impact of this effect by following the method presented in Z16, i.e., we add a systematic error $\Delta_{\rm inst,T}$ to the observed temperature (Kettula et al. 2013; Schellenberger et al. 2015), which is given by $\Delta_{\rm inst,T} = (T - T^{0.889})/T$.

Thermal plasma models and atomic database: The uses of different thermal plasma models and different atomic databases may cause systematic errors in the fittings. Previous studies (e.g., Matsushita et al. 2003; Sato et al. 2011) show that using two sets of the most popular atomic codes/tables, i.e., AtomDB[9] (embedded in the APEC model) and SPEXACT[10] (embedded in the CIE

[9] http://www.atomdb.org/
[10] https://www.sron.nl/astrophysics-spex

Table 3
Best-fit Results

Name	r_{200} (Mpc)	Averaged Temperature[a] (keV)	M_{200} ($10^{14}\,M_{\odot}$)	$M_{\rm gas,200}$ ($10^{13}\,M_{\odot}$)	$L_{\rm X,200}$[b] (10^{44} erg s^{-1})	$R_{\rm eff}$[c]
1E 1455.0+2232	$1.52^{+0.10}_{-0.09}$	$5.23^{+0.26}_{-0.27}$	$5.16^{+1.14}_{-0.85}$	$6.65^{+0.70}_{-0.65}$	$16.74^{+0.46}_{-0.46}$	0.38
A1068	$1.53^{+0.06}_{-0.06}$	$4.48^{+0.16}_{-0.16}$	$4.79^{+0.54}_{-0.56}$	$5.41^{+0.47}_{-0.47}$	$8.07^{+0.25}_{-0.18}$	0.55
A1246	$1.62^{+0.08}_{-0.07}$	$6.37^{+0.43}_{-0.37}$	$5.95^{+0.92}_{-0.76}$	$7.61^{+0.90}_{-1.02}$	$6.60^{+0.32}_{-0.35}$	0.33
A13	$1.51^{+0.06}_{-0.06}$	$4.66^{+0.17}_{-0.18}$	$4.39^{+0.56}_{-0.49}$	$5.92^{+0.50}_{-0.52}$	$2.52^{+0.13}_{-0.13}$	0.52
A133	$1.47^{+0.06}_{-0.06}$	$3.95^{+0.15}_{-0.12}$	$3.89^{+0.49}_{-0.47}$	$4.09^{+0.32}_{-0.31}$	$3.14^{+0.13}_{-0.13}$	0.45
A1413	$1.82^{+0.08}_{-0.07}$	$7.01^{+0.31}_{-0.35}$	$7.94^{+1.07}_{-0.85}$	$9.50^{+0.75}_{-0.88}$	$13.01^{+0.34}_{-0.42}$	0.62
A1689	$1.99^{+0.09}_{-0.07}$	$9.16^{+0.41}_{-0.39}$	$10.79^{+1.49}_{-1.13}$	$14.92^{+0.85}_{-0.93}$	$28.46^{+0.73}_{-0.75}$	0.52
A1775	$1.41^{+0.06}_{-0.05}$	$3.89^{+0.12}_{-0.13}$	$3.47^{+0.47}_{-0.38}$	$4.05^{+0.42}_{-0.46}$	$2.36^{+0.11}_{-0.11}$	0.54
A1795	$1.70^{+0.06}_{-0.05}$	$5.25^{+0.18}_{-0.18}$	$6.06^{+0.62}_{-0.55}$	$8.71^{+0.81}_{-0.72}$	$12.04^{+0.37}_{-0.38}$	0.66
A1835	$1.82^{+0.07}_{-0.05}$	$7.41^{+0.35}_{-0.34}$	$8.93^{+1.14}_{-0.64}$	$13.26^{+1.35}_{-1.00}$	$42.85^{+1.39}_{-1.23}$	0.45
A2029	$2.17^{+0.08}_{-0.09}$	$5.90^{+0.20}_{-0.20}$	$12.77^{+1.47}_{-1.47}$	$13.90^{+1.19}_{-1.01}$	$20.28^{+0.69}_{-0.63}$	0.01
A209	$1.80^{+0.09}_{-0.07}$	$6.98^{+0.32}_{-0.31}$	$8.29^{+1.38}_{-0.98}$	$12.18^{+1.84}_{-1.40}$	$13.60^{+0.60}_{-0.67}$	0.64
A2142	$2.18^{+0.06}_{-0.05}$	$8.03^{+0.14}_{-0.14}$	$13.07^{+1.03}_{-0.93}$	$20.66^{+1.63}_{-1.22}$	$26.70^{+0.67}_{-0.68}$	0.72
A2163	$2.88^{+0.11}_{-0.15}$	$12.08^{+0.41}_{-0.50}$	$33.39^{+4.13}_{-4.91}$	$50.48^{+4.73}_{-6.54}$	$60.15^{+2.55}_{-4.11}$	0.40
A2199	$1.38^{+0.06}_{-0.05}$	$3.96^{+0.15}_{-0.14}$	$3.14^{+0.40}_{-0.33}$	$3.21^{+0.28}_{-0.23}$	$3.53^{+0.13}_{-0.10}$	0.69
A2204	$1.91^{+0.07}_{-0.07}$	$7.18^{+0.29}_{-0.33}$	$9.27^{+1.11}_{-0.93}$	$13.15^{+1.39}_{-1.27}$	$32.06^{+1.04}_{-1.06}$	0.62
A2255	$1.51^{+0.10}_{-0.09}$	$5.77^{+0.30}_{-0.30}$	$4.34^{+0.89}_{-0.71}$	$4.33^{+1.31}_{-0.91}$	$4.51^{+0.29}_{-0.30}$	0.56
A2319	$2.17^{+0.08}_{-0.07}$	$8.28^{+0.20}_{-0.24}$	$12.51^{+1.34}_{-1.13}$	$19.99^{+2.00}_{-1.67}$	$18.37^{+0.72}_{-0.61}$	0.76
A2597	$1.36^{+0.05}_{-0.05}$	$3.56^{+0.11}_{-0.12}$	$3.14^{+0.38}_{-0.33}$	$3.50^{+0.24}_{-0.24}$	$5.43^{+0.14}_{-0.12}$	0.55
A2667	$1.80^{+0.08}_{-0.07}$	$6.89^{+0.31}_{-0.31}$	$8.34^{+1.15}_{-0.98}$	$10.58^{+1.16}_{-1.27}$	$23.27^{+0.72}_{-0.82}$	0.50
A3158	$1.56^{+0.07}_{-0.07}$	$4.89^{+0.15}_{-0.14}$	$4.67^{+0.69}_{-0.57}$	$5.12^{+0.71}_{-0.63}$	$4.63^{+0.22}_{-0.22}$	0.67
A3266	$1.53^{+0.14}_{-0.21}$	$6.34^{+0.46}_{-0.47}$	$4.42^{+1.34}_{-1.56}$	$6.57^{+2.60}_{-2.74}$	$7.45^{+0.55}_{-0.53}$	0.33
A383	$1.55^{+0.08}_{-0.08}$	$4.78^{+0.21}_{-0.18}$	$5.19^{+0.80}_{-0.73}$	$5.76^{+0.41}_{-0.43}$	$8.29^{+0.24}_{-0.23}$	0.77
A478	$1.87^{+0.09}_{-0.09}$	$6.29^{+0.25}_{-0.30}$	$8.25^{+1.21}_{-1.12}$	$10.10^{+1.11}_{-1.00}$	$25.62^{+0.58}_{-0.60}$	0.44
A644	$1.82^{+0.05}_{-0.05}$	$6.51^{+0.20}_{-0.22}$	$7.42^{+0.62}_{-0.62}$	$11.33^{+0.61}_{-0.71}$	$11.12^{+0.34}_{-0.34}$	0.63
A68	$1.68^{+0.08}_{-0.09}$	$6.72^{+0.36}_{-0.38}$	$7.03^{+1.05}_{-1.06}$	$9.72^{+1.36}_{-1.98}$	$11.94^{+0.54}_{-0.60}$	0.47
A773	$1.74^{+0.09}_{-0.08}$	$7.27^{+0.34}_{-0.31}$	$7.42^{+1.18}_{-0.97}$	$9.48^{+1.29}_{-1.18}$	$12.93^{+0.47}_{-0.56}$	0.55
AS1101	$1.13^{+0.05}_{-0.04}$	$2.44^{+0.08}_{-0.08}$	$1.76^{+0.23}_{-0.18}$	$2.17^{+0.12}_{-0.11}$	$2.35^{+0.05}_{-0.05}$	0.69
Centaurus Cluster	$1.25^{+0.06}_{-0.04}$	$2.91^{+0.11}_{-0.11}$	$2.33^{+0.33}_{-0.24}$	$2.41^{+0.23}_{-0.21}$	$1.05^{+0.04}_{-0.07}$	0.28
Cl 0016+16	$1.74^{+0.09}_{-0.07}$	$9.36^{+0.52}_{-0.51}$	$10.68^{+1.74}_{-1.27}$	$15.38^{+2.89}_{-2.03}$	$36.76^{+1.66}_{-1.24}$	0.46
Cl 0024+17	$1.14^{+0.05}_{-0.05}$	$3.41^{+0.20}_{-0.20}$	$2.52^{+0.37}_{-0.30}$	$3.37^{+0.45}_{-0.53}$	$2.85^{+0.23}_{-0.23}$	0.52
Coma Cluster	$1.96^{+0.09}_{-0.10}$	$7.76^{+0.25}_{-0.23}$	$9.00^{+1.36}_{-1.26}$	$10.47^{+1.38}_{-1.09}$	$9.07^{+0.32}_{-0.31}$	0.55
ESO 306-G 017 group	$1.14^{+0.05}_{-0.06}$	$2.43^{+0.12}_{-0.12}$	$1.77^{+0.24}_{-0.27}$	$1.60^{+0.17}_{-0.16}$	$0.59^{+0.04}_{-0.04}$	0.47
HydraA Cluster	$1.32^{+0.04}_{-0.04}$	$3.27^{+0.13}_{-0.15}$	$2.84^{+0.30}_{-0.27}$	$4.05^{+0.30}_{-0.30}$	$5.12^{+0.13}_{-0.14}$	0.68
Perseus Cluster	$1.83^{+0.06}_{-0.07}$	$6.12^{+0.14}_{-0.15}$	$7.26^{+0.81}_{-0.78}$	$9.37^{+0.57}_{-0.60}$	$12.48^{+0.25}_{-0.21}$	0.60
PKS 0745−191 Cluster	$2.10^{+0.12}_{-0.10}$	$8.15^{+0.35}_{-0.37}$	$11.89^{+2.21}_{-1.59}$	$14.99^{+1.46}_{-1.47}$	$30.73^{+0.93}_{-0.87}$	0.71
RXC J0605.8−3518	$1.60^{+0.08}_{-0.08}$	$4.87^{+0.19}_{-0.21}$	$5.36^{+0.82}_{-0.72}$	$6.28^{+0.65}_{-0.64}$	$8.14^{+0.23}_{-0.33}$	0.71
RXC J1825.3+3026	$1.52^{+0.08}_{-0.08}$	$5.58^{+0.21}_{-0.23}$	$4.30^{+0.74}_{-0.64}$	$4.54^{+1.03}_{-0.97}$	$3.07^{+0.25}_{-0.26}$	0.57
RXC J2234.5−3744	$1.76^{+0.07}_{-0.06}$	$7.75^{+0.36}_{-0.38}$	$7.24^{+0.93}_{-0.69}$	$10.34^{+0.89}_{-1.26}$	$13.11^{+0.36}_{-0.42}$	0.63
RX J1120.1+4318	$1.10^{+0.07}_{-0.08}$	$4.70^{+0.38}_{-0.36}$	$2.83^{+0.62}_{-0.60}$	$2.96^{+0.78}_{-0.69}$	$10.50^{+0.55}_{-0.67}$	0.50
RX J1159.8+5531	$0.93^{+0.04}_{-0.03}$	$1.67^{+0.06}_{-0.06}$	$1.00^{+0.12}_{-0.10}$	$0.80^{+0.07}_{-0.05}$	$0.24^{+0.01}_{-0.01}$	0.27
RX J1334.3+5030	$1.16^{+0.08}_{-0.08}$	$4.84^{+0.41}_{-0.36}$	$3.44^{+0.77}_{-0.70}$	$4.22^{+1.35}_{-1.32}$	$7.10^{+0.63}_{-0.74}$	0.50
RX J1347.5−1145	$2.11^{+0.11}_{-0.10}$	$12.19^{+0.73}_{-0.53}$	$17.14^{+2.95}_{-2.21}$	$23.61^{+2.22}_{-2.15}$	$103.48^{+3.26}_{-3.16}$	0.36
UGC 03957 Cluster	$1.06^{+0.03}_{-0.03}$	$2.23^{+0.08}_{-0.08}$	$1.45^{+0.12}_{-0.13}$	$1.12^{+0.08}_{-0.09}$	$0.69^{+0.03}_{-0.03}$	0.61
Virgo Cluster	$1.08^{+0.03}_{-0.03}$	$2.21^{+0.06}_{-0.05}$	$1.48^{+0.12}_{-0.12}$	$1.03^{+0.09}_{-0.08}$	$0.42^{+0.02}_{-0.02}$	0.52
ZwCl 1215.1+0400	$1.74^{+0.07}_{-0.06}$	$6.15^{+0.20}_{-0.21}$	$6.51^{+0.79}_{-0.69}$	$8.39^{+0.61}_{-0.77}$	$5.26^{+0.27}_{-0.23}$	0.66
ZwCl 3146	$1.90^{+0.10}_{-0.08}$	$7.49^{+0.40}_{-0.31}$	$10.35^{+1.77}_{-1.21}$	$13.56^{+0.90}_{-0.92}$	$34.68^{+0.76}_{-0.93}$	0.69

Notes.
[a] The volume-averaged temperature is calculated for the $0.2r_{500}$–$0.5r_{500}$ region using the best-fit temperature profile.
[b] $L_{\rm X,200}$ is the X-ray luminosity within r_{200} calculated in the 0.1–50 keV range.
[c] $R_{\rm eff}$ is used to describe the goodness of fitting (Equation (19)).

model, which is updated from the MEKAL model), will result in a limited difference in gas temperature measurements, which is, however, typically smaller than the statistics error. Mernier et al. (2020) have compared these two models by simulating fake spectra with one of them and then fit the spectra with the other, and they found that the temperatures obtained with the two models show a difference of $\sim$0.05 keV when $T < 1$ keV, or a difference of $\lesssim$5% when $T \geqslant 1$ keV. Therefore, we have added a systematic error $\Delta_{\rm atom,T} = 0.05$ KeV if $T < 1$ keV or $\Delta_{\rm atom,T} = 0.05T$ if $T \geqslant 1$ keV to the observed temperature.

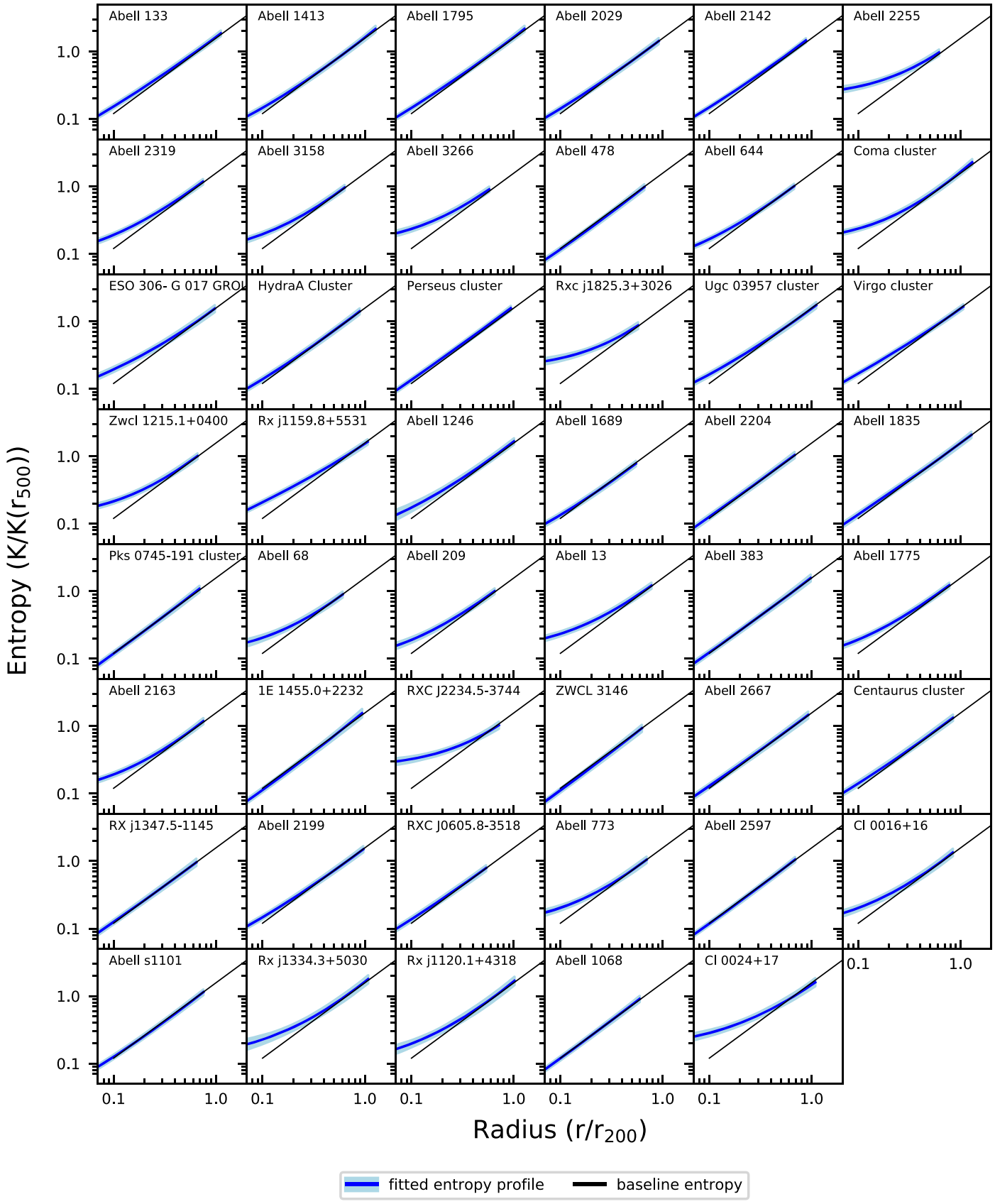

Figure 1. Gas entropy profiles derived from the converged MCMC chains (blue lines), together with the 68% error range (shaded regions). The simulation-predicted profiles (black line) are also plotted for comparison. All the profiles have been scaled by r_{200} and $K(r_{500})$).

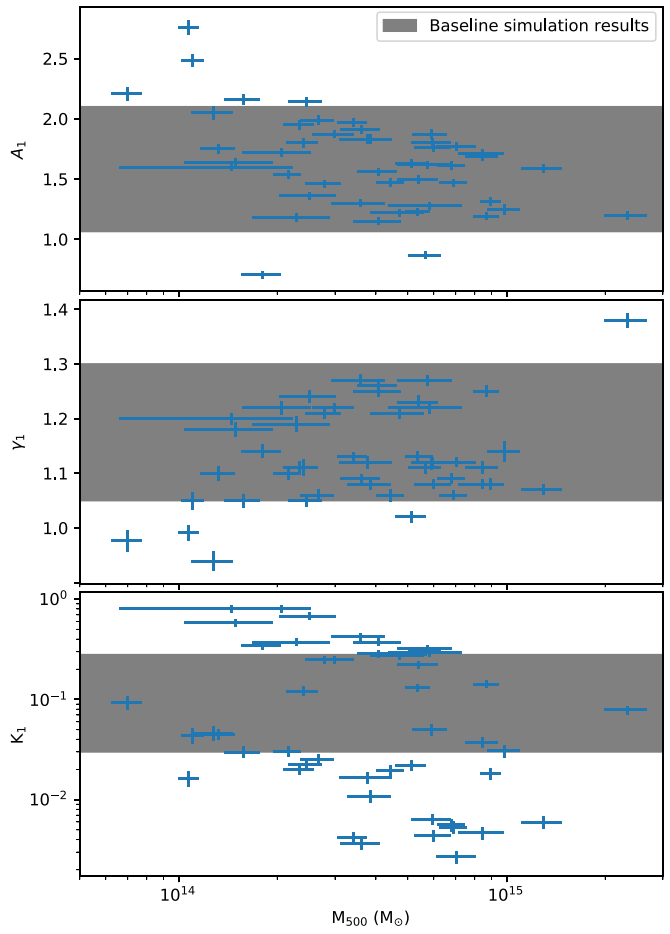

Figure 2. Best-fit parameters of the power-law entropy model A_1 (top panel), γ_1 (middle panel), and K_1 (bottom panel) with their respective errors as functions of M_{500}. The shaded regions show the predictions from baseline simulations (e.g., Tozzi & Norman 2001; Voit et al. 2005).

Metal abundance in outer regions: Due to the limited S/N, the abundance of the outer regions cannot be tightly constrained in many cases. Thus, it is often fixed to typical values such as 0.3 solar or to the abundance of the adjacent inner region. Since the measurements of metal abundance and gas temperature are coupled, the uncertainties in the measurement of the abundance will be transferred to the measurement of gas temperature, which is typically $\lesssim$3% as found by Vikhlinin et al. (2005) (see also Su et al. 2015; Lakhchaura et al. 2016). We have added the error $\Delta_{\rm Aout,T} = 0.03T$ accordingly to the observed temperature of the corresponding outer regions.

Nonequilibrium between electron and proton populations: As proposed by Hoshino et al. (2010), it is possible that the electrons may not be in thermal equilibrium with the protons near the virial radius, which will introduce a systematic error if the thermal equilibrium state is assumed in the model. Currently, no firm observational evidence has been presented to support this idea, and it is estimated that within r_{100} the difference between electron and proton temperature is less than 1% (Wong & Sarazin 2009). Therefore, we add the systematic error $\Delta_{\rm pe,T} = 0.01T$ to the temperatures measured outside r_{500}.

Calculation of two-dimensional temperature: In Section 4 we have modeled the two-dimensional temperature using the method of Mazzotta et al. (2004) (Equation (14)) in the RTI model fitting. This method, however, will lead to at most 10% systematic errors (Mazzotta et al. 2004). We then add $\Delta_{\rm 2d,T} = 0.1T$ to the two-dimensional temperatures.

Possible multiphase gas in the central region: In the cases when a single-phase temperature model is used (Section 3), it is possible that there exists an unresolved cool phase gas, the absence of which may cause a small systematic error in the spectral fitting. In order to estimate the possible model bias in such cases, we use the XSPEC command `fakeit` to create a test spectrum that consists of two APEC components. The temperature of the cool component is set to be 0.8 keV, while that of the hot phase is set to be 2.0, 5.0, and 10.0 keV, respectively. The abundances of both phases are set to be 0.4 solar, and the normalization of the cool component is determined in such a way that the cool phase accounts for 3% of the total emission. We fit the test spectrum with a single-APEC model and find that in all cases the systematic errors less than 1% in measuring the temperature of the single-APEC model will arise when the cool phase component is ignored in the spectral fitting. Thus, we have decided to add an additional systematic error $\Delta_{\rm multi,T} = 0.01T$ to the ICM temperature measured within the innermost 50 kpc when the single temperature model is applied.

5.1.2. Systematic Errors in Measuring X-Ray Surface Brightness

Instrument calibration: As shown in Schellenberger et al. (2015) and Kettula et al. (2013), for a given target the difference of the X-ray surface brightness measured via Chandra, XMM-Newton, and Suzaku can be up to about 10% owing to the effective area calibration uncertainties. Therefore, we have added a systematic error $\Delta_{\rm inst,S} = 0.1S_{\rm obs}$ to the observed surface brightness.

Calculation of cooling function: The gas emissivity depends linearly on the cooling function (Equation (15)), which further depends on the gas metal abundance. Systematic errors will rise if the metal abundances cannot be well constrained in the outer regions (Section 5.1.1). By altering the abundance in the typical range (0.1–0.5; Lovisari & Reiprich 2019), we find that the cooling function is shifted by about 5%. Hence, we adopt a systematic error $\Delta_{\rm abund,S} = 0.05S_{\rm model}$ to the calculated surface brightness profile to account for this effect.

5.2. The Necessity of RTI Model Parameters

An empirical description of gas temperature and surface brightness requires about 10 free parameters (~4–7 for temperature; e.g., Allen et al. 2001; Vikhlinin et al. 2006; Zhang et al. 2006; ~3–6 for the β or double-β model of the surface brightness), although the RTI model and some previous studies (e.g., Ostriker et al. 2005; Patej & Loeb 2015; Z16) demonstrated the possible necessity to include more free parameters for describing the physical processes behind. In order to evaluate whether all the parameters listed in Table 2 are necessary for the current RTI model, we have compared the best-fit model predictions obtained from the RTI model fitting in the following five representative cases: (1) best-fit results as given in Section 4.2 (21 free parameters); (2) five parameters related to the gas clumping profile (i.e., c_1, c_2, c_3, c_4, and c_5; parameter group A) are neglected in the fitting, and $C(r)$ are set to be 1 (16 free parameters); (3) in addition to case 2, three parameters related to the nonthermal pressure (i.e., A, B, and γ; parameter group B) are neglected in the fitting, and η (r) are set to be 1 (13 free parameters); (4) in addition to case 3, values of two parameters related to the accretion shock (i.e., $r_{\rm shock}$

Table 4
Sample-averaged $R_{\rm eff}$ for Cases Tested in Section 5.2

Group A	Group B	Group C	Group D	Group E	$R_{\rm eff}$
c_1 to c_5	A, B, γ	$r_{\rm shock}$, Γ	N_2, N_3, $C_{\rm w}$	ρ_0, r_s, δ_1, δ_2, A_0, γ_0, K_0, f_g	
				✓	−1.20 (case 5)
✓				✓	−0.22
	✓			✓	−0.30
		✓		✓	−0.31
			✓	✓	0.20 (case 4)
✓	✓			✓	−0.18
✓		✓		✓	−0.18
✓			✓	✓	0.21
	✓	✓		✓	−0.12
	✓		✓	✓	0.17
		✓	✓	✓	0.45 (case 3)
✓	✓	✓		✓	0.31
✓	✓		✓	✓	0.28
	✓	✓	✓	✓	0.51 (case 2)
✓	✓	✓	✓	✓	0.53 (case 1)

Note. Parameters that were included and set free in the fitting are marked by ✓ for each case.

and Γ; parameter group C) are fixed to the averaged values derived from the observation of Patej & Loeb (2015) (11 free parameters); (5) in addition to case 4, values of three parameters related to the energy conservation (i.e., N_2, N_3, and C_w; parameter group D) are fixed to the theoretical or simulated values that have been accepted and used among astronomical community (e.g., Chaudhuri et al. 2012; Nelson et al. 2014; Z16) (8 free parameters; parameter group E).

According to the definition of model efficiency, a larger value of $R_{\rm eff}$ indicates a better model fit within the range of $(-\infty, 1]$. An acceptable model fit is acquired when $R_{\rm eff} \gtrsim 0$, and the model best describes the observation when $R_{\rm eff} = 1$ is achieved (e.g., Nash & Sutcliffe 1970; Engeland & Gottschalk 2002). The derived sample-averaged $R_{\rm eff}$ (Table 4) for the five cases are 0.53, 0.51, 0.45, 0.20, and −1.2, respectively, where cases 1−4 gives acceptable fits and case 1 best describes the observation among the five cases. In addition, we have also tested cases given by altering the order of neglecting or fixing to the parameters described in cases 2 to 5, and all of them yielded averaged $R_{\rm eff}$ smaller than 0.53 (Table 4), the averaged $R_{\rm eff}$ of the original best-fit in Section 4, suggesting that among all cases, the original model (case 1) as introduced in Section 4 best describes the observation. The most consequential parameter group that improves $R_{\rm eff}$ are the energy conservation parameters (group D), and the minimum number of parameters needed to achieve $R_{\rm eff} \gtrsim 0$ is 11, as used in case 4.

To give a further evaluation on the statistical significance, we used the Akaike Information Criterion (AIC; Akaike 1974) to decide which one best describes the observations. The AIC, which has been widely used as a model selection criterion (e.g., Aho et al. 2014), is defined as

$$\mathrm{AIC} = 2k - 2\ln(L), \tag{24}$$

where k is the total number of all model parameters and L is the likelihood function that is defined to characterize the goodness of fit of the model to the observed data (Equation (18)). Given two sets of model predictions, the relative likelihood L_R of them is calculated as $\exp((\mathrm{AIC}_1 - \mathrm{AIC}_2)/2)$ and is used in the likelihood ratio test to judge which prediction is better. In the likelihood ratio test we set the threshold p-value to be 0.05, a value commonly used in astronomical literature for the significance test. When $L_R < 0.05$, which corresponds to $\mathrm{AIC}_1 - \mathrm{AIC}_2 \lesssim -6$, the model prediction with a smaller AIC value is regarded as the better one to describe the data set. Otherwise, neither prediction can be regarded as better than the other. In Table 5 we list the AIC values calculated in the above five cases for all sample members. The sample-averaged AIC value of the five cases are 2268, 2277, 2305, 2376, and 2579, respectively. The AIC differences between cases 2−5 and case 1 are −9, −37, −108, and −311 respectively, providing statistical evidence for case 1's superiority over cases 2−5. Therefore, albeit the seemingly large number of free parameters (e.g., Burnham & Anderson 2002; Claeskens 2016), the best-fit model in Section 4 can be considered as the appropriate one to describe the observation, suggesting that all the RTI model parameters are necessary in order to describe the corresponding physical processes in the fitting (Section 4.2).

5.3. The Impact of Gas Clumping

5.3.1. Gas Clumping Signal in the Center of Galaxy Clusters and Groups

The sample-averaged best-fit clumping profile has a significant signal inside $\sim 0.1 r_{500}$ (see Figure 3) as expected from cosmological simulations (e.g., Vazza et al. 2013) and found in the observations of the Perseus and Coma Clusters (e.g., Churazov et al. 2012; Zhuravleva et al. 2015). Since such clumping signals appear in the simulation when effects of the AGN activity and the radiative cooling are taken into account, we propose that accumulated effects of the AGN historical feedback and the radiative cooling have contributed to the central clumping signal. In order to verify the assumption, we calculate the electron−ion equilibrium timescale ($t_{\rm ei}$), the sound-crossing timescale ($t_{\rm s}$), and the buoyancy timescale ($t_{\rm b}$) at $0.05 r_{500}$ of sample members, the longest of which can be used as an indicator of the relaxation time for the gas at the cluster center. Following Hoshino et al. (2010), we calculate $t_{\rm ei}$ as

$$t_{\rm ei}(r) \simeq 2.0 \times 10^8\ \mathrm{yr} \frac{(T(r)/10^8\ \mathrm{K})^{3/2}}{(n_{\rm p}(r)/10^{-3}\ \mathrm{cm}^{-3})(\ln\Lambda_c(r)/40)}, \tag{25}$$

where $\ln\Lambda_c(r)$ is the Coulomb logarithm, which is calculated as

$$\ln\Lambda_c(r) = 30 - \ln\left(\frac{n_{\rm e}(r)^{1/2}}{\mathrm{cm}^{-3}} \frac{T(r)^{-3/2}}{\mathrm{eV}}\right). \tag{26}$$

Here $t_{\rm s}$ and $t_{\rm b}$ are calculated following Gitti et al. (2012) as $t_{\rm s}(r) = r/\sqrt{5k_{\rm b}T(r)/3\mu m_{\rm p}}$ and $t_{\rm b}(r) = r/\sqrt{2GM(<r)R_{\rm cs}/r^2}$, where $R_{\rm cs}$ is the scale of gas clumping at $0.05\ r_{500}$ and is estimated to be 10 kpc. We plot $t_{\rm ei}$, $t_{\rm s}$, and $t_{\rm b}$ as functions of the clumping factor $(C(r)^{0.5} - 1)$ at $0.05\ r_{500}$ for each sample member in Figure 4. The correlations between the three timescales ($t_{\rm ei}$, $t_{\rm s}$, and $t_{\rm b}$) and the clumping factor are 0.82 ± 0.07, -0.62 ± 0.06, and 0.70 ± 0.09, respectively. As shown in Figure 4, $t_{\rm b}$ is the largest out of the three timescales, which is on the order of the AGN cycling time ($\sim 10^7$–10^8 yr; Blanton et al. 2010), and sample members with longer $t_{\rm b}$ generally have larger clumping factors at

Table 5
AIC Values for the Model Predictions Obtained in the Five Cases Described in Section 5.2

Name[a]	Case 1	Case 2	Case 3	Case 4	Case 5
1E 1455.0+2232	2351.8	2326.8	2426.8	2490.7	2427.5
A1068	2403.3	2384.5	2414.6	2620.9	3283.4
A1246[1]	2515.6	2600.8	2659.7	2684.7	2747.4
A13	2336.0	2340.2	2348.7	2335.6	2431.5
A133[1]	1876.0	1886.2	1899.4	1900.5	2560.4
A1413	2149.7	2144.9	2160.6	2240.2	2261.4
A1689	2583.3	2540.9	2584.7	2577.4	2832.3
A1775	2276.2	2242.5	2268.1	2282.4	2386.2
A1795[1]	1616.0	1631.2	1635.2	1761.2	2140.5
A1835[1]	2518.2	2526.2	2526.7	2710.0	2952.5
A2029[1]	2388.5	2398.3	2423.3	2514.3	2783.6
A209[1]	2361.5	2390.4	2397.0	2425.0	2437.3
A2142[1]	1097.2	1169.2	1202.5	1220.9	1569.0
A2163	2464.5	2440.0	2450.3	2463.1	2469.5
A2199	2230.6	2223.7	2269.9	2307.6	3124.1
A2204[1]	2243.7	2250.1	2272.2	2412.8	2638.5
A2255[1]	2493.1	2562.1	2579.8	2606.0	2683.6
A2319[1]	1584.8	1631.0	1630.1	1626.0	1712.4
A2597	2325.5	2323.4	2383.0	2598.9	3183.7
A2667	2366.9	2350.3	2384.7	2543.1	2548.4
A3158	2541.7	2539.4	2576.7	2594.1	2623.7
A3266	2548.4	2535.6	2552.8	2568.7	2572.9
A383	2294.7	2291.4	2337.4	2325.9	3066.6
A478	2102.1	2064.1	2102.7	2209.1	2266.2
A644[1]	2471.6	2557.5	2621.3	2701.7	2854.1
A68[1]	2418.9	2461.5	2482.3	2516.2	2510.5
A773	2465.0	2451.8	2486.7	2507.1	2526.0
AS1101[1]	2213.7	2244.4	2324.1	2613.4	2904.6
Centaurus Cluster	2164.6	2170.1	2176.3	2184.4	3283.0
Cl 0016+16[1]	2127.7	2150.1	2122.4	2130.6	2125.5
Cl 0024+17	2287.5	2288.0	2307.2	2307.6	2306.8
Coma Cluster	1592.6	1548.7	1609.4	1656.0	1669.2
ESO 306-G 017 group	2402.5	2374.9	2412.0	2472.6	2532.2
HydraA Cluster	2182.3	2148.5	2176.7	2241.4	2195.1
Perseus Cluster[1]	2104.1	2259.0	2279.3	2355.8	2430.3
PKS 0745−191 Cluster[1]	2338.8	2345.4	2392.7	2662.8	3247.9
RXC J0605.8−3518	2371.2	2363.4	2400.1	2508.0	2760.9
RXC J1825.3+3026	2578.5	2578.9	2600.2	2600.7	2625.1
RXC J2234.5−3744	2429.4	2403.6	2447.1	2392.4	2468.8
RX J1120.1+4318[1]	1958.2	2036.1	2000.9	2067.8	2011.2
RX J1159.8+5531	2439.4	2411.6	2417.8	2393.1	2720.0
RX J1334.3+5030	2234.7	2232.4	2235.8	2285.7	2316.0
RX J1347.5−1145[1]	2512.1	2555.6	2591.1	2910.0	3188.8
UGC 03957 Cluster	2348.9	2336.3	2364.0	2391.1	2524.1
Virgo Cluster[1]	2305.2	2316.7	2367.6	2328.9	2446.9
ZwCl 1215.1+0400	2527.4	2533.4	2575.9	2591.2	2621.5
ZwCl 3146	2442.6	2439.4	2466.2	2848.0	3259.3

Note.
[a] The superscripts 1 indicate that the effect of gas clumping is important and can significantly improve the fittings by including it in the model.

$0.05r_{500}$. This result supports our argument that the accumulated effects of AGN historical feedback have contributed to the central clumping signal since it will be more difficult for the sample member with a larger equilibrium time to become relaxed after the AGN activity disturbs the core region.

5.3.2. Is the Gas Clumping Effect Common in Clusters and Groups?

Cosmological simulations of, e.g., Nagai & Lau (2011) and Vazza et al. (2013), predicted that at cluster or group outskirts

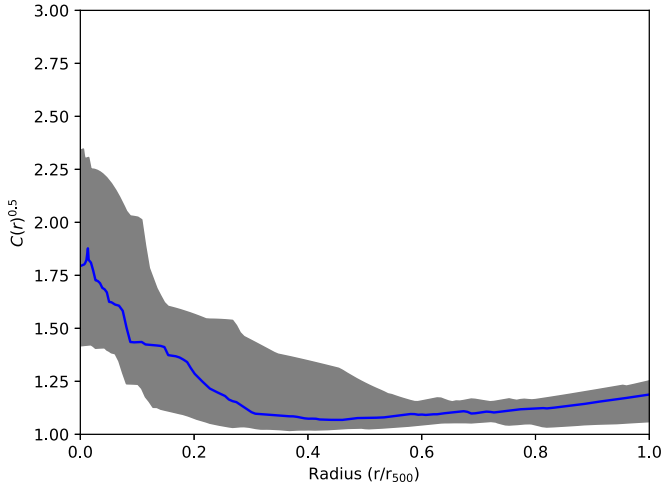

Figure 3. Averaged clumping factor as a function of radius for all sample members. The shaded area represents the 68% uncertainty range.

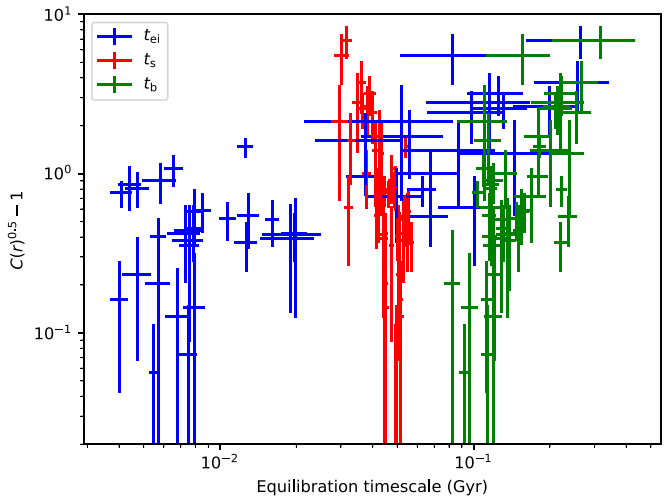

Figure 4. Gas clumping factor as a function of the electron−ion equilibration (blue; t_{ei}), sound-crossing (red; t_s), and buoyancy (green; t_b) timescale at $0.05r_{500}$ for all sample members.

the ICM is inhomogeneous and apparently deviates from the hydrostatic equilibrium. In the past decade corresponding studies, which mainly focused on the effects gas clumping, have been conducted based on the observations of Chandra (e.g., Churazov et al. 2012; Zhuravleva et al. 2015), ROSAT (e.g., Eckert et al. 2012, 2015), and XMM-Newton (e.g., Eckert et al. 2019; Ghirardini et al. 2019). In order to investigate what is the major difference between the targets showing clear evidence for gas clumping and those not, and, from another perspective, to answer the question whether or not the gas clumping effect is actually common in clusters and groups, we have divided the targets into two corresponding subsamples, one (subsample A) containing 19 targets (8 of which are included in the W12a sample) that show significant improvement when the effect of gas clumping is considered in the model (marked with the superscript "1" in Table 5), and the other (subsample B) containing the remaining 28 targets.

We have attempted to compare the redshifts, the gas temperatures averaged between $0.2r_{500}$ and $0.5r_{500}$, the virial masses, the surface brightness concentrations (i.e., the integrated

surface brightness within $0.2r_{500}$ divided by that within r_{500}), and the 0.7–7.0 keV fluxes integrated inside r_{500} ($f_{\rm X,500}$) of the two subsamples by applying the Kolmogorov–Smirnov test (e.g., Næss 2012). In particular, for each of the physical properties we calculate the empirical cumulative distribution functions (e.g., van der Vaart 1998) $F(x)$ calculated for two subsamples and use them to determine the maximum difference (D_{n_1,n_2}), which is defined as

$$D_{n_1,n_2} = \max_x |F_{n_1}(x) - F_{n_2}(x)|, \quad (27)$$

where n_1 and n_2 are the sizes of the two subsamples, respectively, and $\max_x$ represents the maximum value of the function $|F_{n_1}(x) - F_{n_2}(x)|$ (e.g., for gas temperature) over the domain x. Thus, we may conclude that, at the level of α, where $\alpha = 2\exp(-2c(\alpha)^2)$ and $c(\alpha) = D_{n_1,n_2}\Big/\sqrt{\frac{n_1+n_2}{n_1 n_2}}$, the hypothesis that the two subsamples possess the same properties is rejected (e.g., Knuth 1997). Following Szydłowski et al. (2015), when α is found to be less than the threshold value of 0.05, the two subsamples are regarded to be significantly different. We find that only $f_{\rm X,500}$ shows a significant difference between the two subsamples ($\alpha = 8.0\times10^{-5}$) under this criterion. As shown in Figure 5, where the distributions of target number as a function of $f_{\rm X,500}$ are plotted, the median values are $f^A_{\rm X,500} = 1.5\times10^{-10}$ erg s^{-1} cm^{-2} and $f^B_{\rm X,500} = 1.8\times10^{-11}$ erg s^{-1} cm^{-2} for the two subsamples, respectively.

For the current X-ray missions such as Suzaku, XMM-Newton, and Chandra, the typical background level in 0.7–7.0 keV is of the order of 10^{-6} photons cm^{-2} arcmin^{-2} s^{-2} (e.g., Hoshino et al. 2010; Nakajima et al. 2018). Meanwhile, the typical uncertainties in background modeling and instrument calibration reach about 10%–20% (e.g., Kushino et al. 2002; Gu et al. 2016) and ∼10% (Section 5.1.2), respectively. These yield a detection threshold of 5×10^{-12} erg s^{-1} cm^{-2}, 2×10^{-11} erg s^{-1} cm^{-2}, or 5×10^{-11} erg s^{-1} cm^{-2} for target emission measured within r_{500} to resolve the surface brightness increment caused by the gas clumping effect, if a typical 50 ks observation is performed and the clumping factor $C(r_{500})$ is set to 1.05, 1.2, or 1.5, respectively. It is apparent that unless a target possesses a high $f_{\rm X,500}$, which is typical for the targets in subsample B, it is impossible to reveal any information about gas clumping at $\sim r_{500}$, even if the clumps do exist. In clusters or groups with high X-ray fluxes, it seems that the gas clumping effect is very popular at $\sim r_{500}$.

5.3.3. Detection of Gas Clumps in X-Ray Maps

It will be very interesting to investigate whether or not we are able to resolve gas clumps directly at $\sim r_{500}$ in the observed X-ray maps. By studying the simulated X-ray maps, Vazza et al. (2013) found that gas clumps exist on $\lesssim$50 kpc scales in the outer regions ($\gtrsim r_{500}$) of all simulated galaxy clusters. Based on 21 Chandra observations, Zhuravleva et al. (2015) confirmed the existence of such gas clumps in the central 220 kpc of the Perseus Cluster by analyzing the power spectrum of the X-ray maps. Can this phenomenon be directly observed at the cluster outskirts via imaging analysis? We have searched the Chandra archive[11] for the clusters and groups satisfying the following three criteria: (1) the cluster or group should have been observed out to r_{500} with a full or a nearly full azimuthal coverage, (2) the redshift should be lower than 0.3 to enable the detection of gas clumps on $\lesssim$50 kpc scales, and (3) net photon counts inside a 50×50 kpc^2 region should be more than 200 near r_{500} to guarantee a sufficient sensitivity. We found that only five clusters (i.e., A133, A1795, A1882, A1914, and A2146) meet the first two criteria. Exposures of at least 1×10^6 s at cluster outskirts are necessary, which are not currently available for all these clusters, to satisfy the third criterion. Clearly deep field observations are necessary in the future in order to resolve such gas clumps at $\sim r_{500}$.

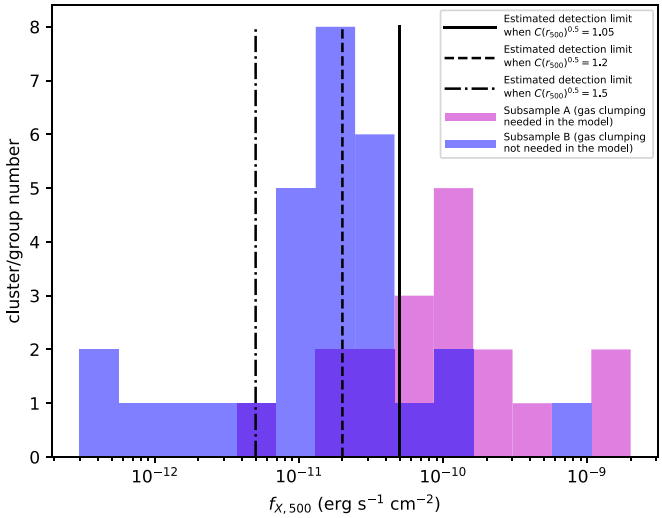

Figure 5. Number distributions of clusters and groups as a function of $f_{\rm X,500}$. Vertical lines show the estimated detection limit for different clumping levels, which are characterized by the clumping factor $C(r_{500})$ (see Figure 3). A 50 ks observations is assumed for current X-ray missions such as Chandra or XMM-Newton.

5.4. Comparison with Previous Works

Our conclusion that the gas entropy profiles of the clusters in our sample are consistent with the power-law prediction of Voit et al. (2005) also agrees with that of Ghirardini et al. (2019), who performed a joint X-ray and Sunyaev–Zel'dovich analysis for a sample of 12 galaxy clusters (10 of these clusters have been included in this work; see Table 1), as well as those of, e.g., Su et al. (2015) and Tchernin et al. (2016), who carried out X-ray image spectroscopic studies on a single target. Apparently these results conflict with the conclusions drawn in a few other studies, such as W12a (all 11 clusters are studied in this work).

Given the fact that in our work the fittings of the gas temperature and X-ray surface brightness profiles among 8 out of 11 W12a clusters show significant improvement when the gas clumping effect is taken into account (see Table 5), it is reasonable to speculate that in W12a the gas density may have been overestimated at $\sim r_{500}$. To verify this speculation, we have tentatively rerun the RTI model fitting for the 11 W12a clusters by switching off the gas clumping effect (i.e., case 2 in Section 5.2). We find that the obtained gas distribution profiles and entropy profiles are consistent with those of W12a (68% confidence level; Figure 6). In fact, W12a, Ghirardini et al. (2019), and other authors have suggested that it is very likely that the flattening of the entropy profiles will arise when the gas clumping effect is not properly considered in the model at $\sim r_{500}$. W12a also pointed out that neglecting the gas clumping effect in the model will cause the excess of gas fraction over the mean cosmic baryon fraction beyond r_{500} (e.g., Simionescu et al. 2011).

[11] https://cxcfps.cfa.harvard.edu/cda/footprint/cdaview.html

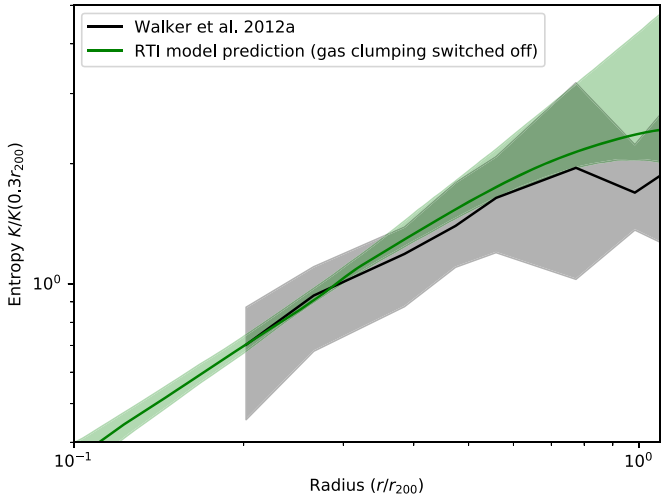

Figure 6. RTI-model-predicted gas entropy profile, which is averaged over 11 W12a clusters and calculated when the gas clumping effect is switched off (green line), along with that of W12a (black line). Shaded areas represent the 68% uncertainty ranges.

5.5. Feedback Energy

Using the derived gas entropy profiles, we are able to study the energy injected into the ICM through the feedback processes. For a small gas element, the total feedback energy is $\Delta E_{\rm feed}(r) = \Delta E_{\rm heating}(r) + \Delta E_{\rm rad}(r)$, where $\Delta E_{\rm heating}(r)$ has been calculated with Equation (8), and $\Delta E_{\rm rad}(r)$ is the radiative loss that can be calculated as a time integration of the X-ray luminosity from t_0 (the age of the universe at $z = 3$) to t_{z0} (the age of the universe at the observation). In order to estimate $\Delta E_{\rm rad}(r)$, we employ the redshift-dependent mass–luminosity relations given in the simulation work of Truong et al. (2018) and the cluster mass evolution provided by Voit et al. (2003, see their Figure 1), i.e.,

$$\Delta E_{\rm rad}(r) = \int_{t_0}^{t_{z0}} f_L(m(t), t)\frac{L_{\rm X}(r)}{f_L(m(t_{z0}), t_{z0})}dt, \quad (28)$$

where $f_L(m, t)$ denotes the luminosity–mass relation at time t, $m(t)$ is the corresponding cluster mass at time t and is constrained by $m(t_{z0}) = M_{500}$, and $L_{\rm X}(r)$ is the luminosity of the gas element at z_0,

$$L_{\rm X}(r) = C(r)n_e(r)n_p(r)\Lambda_{\rm bol}(T, Z)V^*, \quad (29)$$

where $\Lambda_{\rm bol}(T, Z)$ is the cooling function in 0.1–50 keV and V^* is the volume of the gas element.

We plot the calculated sample-averaged feedback energy per gas particle as a function of radius in Figure 7 and find that the feedback energy outside $\sim 0.35r_{200}$ is consistent with 0, suggesting that the preheating is likely to inject no more than 0.5 keV per particle (averaged between $0.35r_{200}$ and r_{500}). Interestingly, the radius $0.35r_{200}$ is similar to the radius within which a central abundance excess, if one exists, is usually found (e.g., Makishima et al. 2001; Lovisari & Reiprich 2019).

The total feedback energy within r_{500} is estimated by integrating the $\Delta E_{\rm feed}(r)$,

$$E_{\rm feed,tot} = \int_0^{r_{500}} 4\pi n_{\rm g} r^2 \Delta E_{\rm feed}(r)/n^* dr. \quad (30)$$

We plot and show the dependence of $E_{\rm feed,tot}$ on cluster mass in Figure 8, in which the distribution of data roughly follows a power-law form. Assuming that the total feedback energy is fully provided by the SMBH sitting in the BCG, we estimate the feedback efficiency $\eta_{\rm feed}$, which is defined as the ratio of feedback energy to the energy corresponding to the rest mass of SMBH ($M_{\rm BH}$). By adopting the M_{500}–$M_{\rm BH}$ relation, derived from a sample of 71 galaxy clusters by Phipps et al. (2019),

$$\log_{10}\left(\frac{M_{\rm BH}}{10^9 M_\odot}\right) = -0.82 + 1.16\log_{10}\left(\frac{M_{500}}{10^{13}M_\odot}\right), \quad (31)$$

we obtained $\eta_{\rm feed} \sim 0.02$ (Figure 8), implying that the black holes may be nonspinning (e.g., Fabian 2012). As a comparison, the feedback efficiency is usually assumed to be in the range of 0.005–0.2 in simulations (e.g., Sijacki & Springel 2007; Puchwein et al. 2008; Sijacki et al. 2008). The estimation of SMBH feedback efficiency will be an upper limit if there exist heating sources other than the SMBHs (e.g., the preheating of gas before it accelerates into the galaxy clusters or groups), or possible mergers that would increase the entropy.

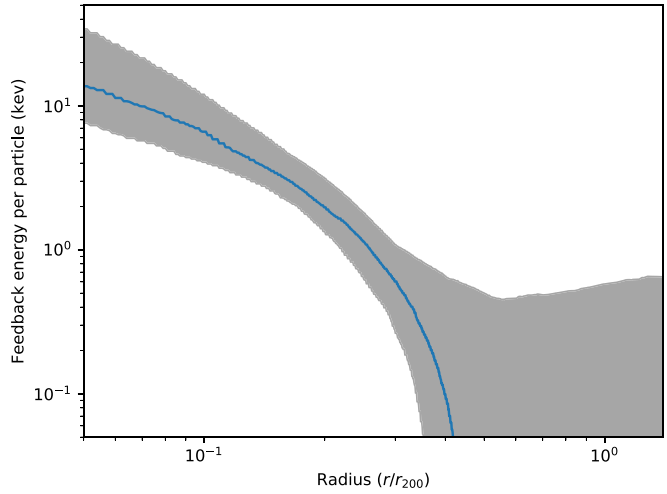

Figure 7. Sample-averaged total feedback energy (blue line) with the 68% uncertainty range (shaded region).

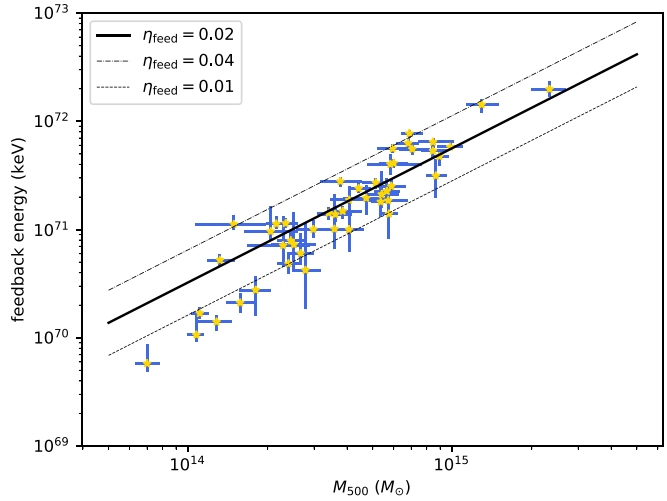

Figure 8. Total feedback energy of clusters or groups in the sample.

6. Summary

We have investigated the entropy profiles of ICM in a sample of 47 galaxy clusters and groups that have been observed out to

at least $\sim r_{500}$ using a physical model, which takes into account the effect of gravitational heating, work done via gas compression, net heat change through nongravitational processes, nonthermal pressure, and the gas clumping. Our model has achieved acceptable fits to all of the sample members, and the best-fit sample-averaged ICM entropy profile is consistent with the power-law prediction from adiabatic simulations near the virial radius. The sample-averaged feedback energy profile derived from the best-fit entropy profile is consistent with zero at the 68% confidence level outside $\sim 0.35 r_{200}$. Based on the relation of M_{500} and the total feedback energy, we suggest that the upper limit of the feedback efficiency is $\sim$0.02 for the SMBH of the BCG, which lies in the range of 0.005–0.2 that is usually used in cosmological simulations.

This work is supported by the Ministry of Science and Technology of China (grant No. 2018YFA0404601) and the National Natural Science Foundation of China (grant Nos. 1197303311, 11835009, 11621303).

ORCID iDs

Zhenghao Zhu https://orcid.org/0000-0001-8443-6095
Haiguang Xu https://orcid.org/0000-0001-9405-0137
Dan Hu https://orcid.org/0000-0003-0450-7960

References

Aho, K., Derryberry, D., & Peterson, T. 2014, Ecology, 95, 631
Akaike, H. 1974, ITAC, 19, 716
Akamatsu, H., Hoshino, A., Ishisaki, Y., et al. 2011, PASJ, 63, S1019
Akamatsu, H., Mizuno, M., Ota, N., et al. 2017, A&A, 600, A100
Allen, S. W., Schmidt, R. W., & Fabian, A. C. 2001, MNRAS, 328, L37
Andreon, S., & Hurn, M. A. 2012, SADM, 6, 15
Bautz, M. W., Miller, E. D., Sanders, J. S., et al. 2009, PASJ, 61, 1117
Blanton, E. L., Clarke, T. E., Sarazin, C. L., et al. 2010, PNAS, 107, 7174
Buote, D. A., Su, Y., Gastaldello, F., et al. 2016, ApJ, 826, 146
Burnham, K. P., & Anderson, D. R. 2002, Model Selection and Multimodel Inference: A Practical Information-theoretic Approach (2nd ed.; Berlin: Springer)
Cavagnolo, K. W., Donahue, M., Voit, G. M., & Sun, M. 2009, ApJS, 182, 12
Chaudhuri, A., Nath, B. B., & Majumdar, S. 2012, ApJ, 759, 87
Churazov, E., Vikhlinin, A., Zhuravleva, I., et al. 2012, MNRAS, 421, 1123
Claeskens, G. 2016, AnRSA, 3, 233
Eckert, D., Ghirardini, V., Ettori, S., et al. 2019, A&A, 621, A40
Eckert, D., Roncarelli, M., Ettori, S., et al. 2015, MNRAS, 447, 2198
Eckert, D., Vazza, F., Ettori, S., et al. 2012, A&A, 541, A57
Engeland, K., & Gottschalk, L. 2002, HESS, 6, 883
Fabian, A. C. 2012, ARA&A, 50, 455
Ghirardini, V., Eckert, D., Ettori, S., et al. 2019, A&A, 621, A41
Gitti, M., Brighenti, F., & McNamara, B. R. 2012, AdAst, 2012, 950641
Grevesse, N., & Sauval, A. J. 1998, SSRv, 85, 161
Gu, L., Wen, Z., Gandhi, P., et al. 2016, ApJ, 826, 72
Hastings, W. K. 1970, Biometrika, 57, 97
Hoshino, A., Henry, J. P., Sato, K., et al. 2010, PASJ, 62, 371
Hudson, D. S., Mittal, R., Reiprich, T. H., et al. 2010, A&A, 513, A37
Ichikawa, K., Matsushita, K., Okabe, N., et al. 2013, ApJ, 766, 90
Iqbal, A., Kale, R., Majumdar, S., et al. 2017, JApA, 38, 68
Kaiser, N. 1986, MNRAS, 222, 323
Kalberla, P. M. W., Burton, W. B., Hartmann, D., et al. 2005, A&A, 440, 775
Kardar, M. 2007, Statistical Physics of Particles (Cambridge: Cambridge Univ. Press)
Kawaharada, M., Okabe, N., Umetsu, K., et al. 2010, ApJ, 714, 423
Kettula, K., Nevalainen, J., & Miller, E. D. 2013, A&A, 552, A47
Khatri, R., & Gaspari, M. 2016, MNRAS, 463, 655
Knuth, D. E. 1997, The Art of Computer Programming, Vol. 2 (3rd ed.; Boston, MA: Addison-Wesley Longman)
Kotov, O., & Vikhlinin, A. 2005, ApJ, 633, 781
Kushino, A., Ishisaki, Y., Morita, U., et al. 2002, PASJ, 54, 327
Lakhchaura, K., Saini, T. D., & Sharma, P. 2016, MNRAS, 460, 2625
Lapi, A., Fusco-Femiano, R., & Cavaliere, A. 2010, A&A, 516, A34
Lovell, M. R., Pillepich, A., Genel, S., et al. 2018, MNRAS, 481, 1950
Lovisari, L., & Reiprich, T. H. 2019, MNRAS, 483, 540
Makishima, K., Ezawa, H., Fukuzawa, Y., et al. 2001, PASJ, 53, 401
Matsushita, K., Finoguenov, A., & Böhringer, H. 2003, A&A, 401, 443
Mazzotta, P., Rasia, E., Moscardini, L., et al. 2004, MNRAS, 354, 10
Mernier, F., Werner, N., Lakhchaura, K., et al. 2020, AN, 341, 203
Miller, E. D., Bautz, M., George, J., et al. 2012, in AIP Conf. Ser. 1427, SUZAKU 2011: Exploring the X-ray Universe: Suzaku and Beyond, ed. R. Petre, K. Mitsuda, & L. Angelini (Melville, NY: AIP), 13
Morandi, A., & Cui, W. 2014, MNRAS, 437, 1909
Morandi, A., & Sun, M. 2016, MNRAS, 457, 3266
Næss, S. K. 2012, A&A, 538, A17
Nagai, D., & Lau, E. T. 2011, ApJL, 731, L10
Nakajima, H., Maeda, Y., Uchida, H., et al. 2018, PASJ, 70, 21
Nash, J. E., & Sutcliffe, J. V. 1970, JHyd, 10, 282
Navarro, J. F., Frenk, C. S., & White, S. D. M. 1997, ApJ, 490, 493
Nelson, K., Lau, E. T., & Nagai, D. 2014, ApJ, 792, 25
Okabe, N., Umetsu, K., Tamura, T., et al. 2014, PASJ, 66, 99
Ostriker, J. P., Bode, P., & Babul, A. 2005, ApJ, 634, 964
Panagoulia, E. K., Fabian, A. C., & Sanders, J. S. 2014, MNRAS, 438, 2341
Patej, A., & Loeb, A. 2015, ApJL, 798, L20
Phipps, F., Bogdán, Á., Lovisari, L., et al. 2019, ApJ, 875, 141
Planelles, S., Borgani, S., Dolag, K., et al. 2013, MNRAS, 431, 1487
Pointecouteau, E., Arnaud, M., Kaastra, J., et al. 2004, A&A, 423, 33
Press, W. H., & Schechter, P. 1974, ApJ, 187, 425
Puchwein, E., Sijacki, D., & Springel, V. 2008, ApJL, 687, L53
Reiprich, T. H., Hudson, D. S., Zhang, Y.-Y., et al. 2009, A&A, 501, 899
Roncarelli, M., Ettori, S., Dolag, K., et al. 2006, MNRAS, 373, 1339
Sato, K., Matsushita, K., Tamura, T., et al. 2014, in Suzaku-MAXI 2014: Expanding the Frontiers of the X-ray Universe, ed. M. Ishida, R. Petre, & K. Mitsuda, 414
Sato, K., Matsushita, K., Yamasaki, N. Y., et al. 2014, PASJ, 66, 85
Sato, T., Matsushita, K., Ota, N., et al. 2011, PASJ, 63, S991
Sato, T., Sasaki, T., Matsushita, K., et al. 2012, PASJ, 64, 95
Schellenberger, G., Reiprich, T. H., Lovisari, L., Nevalainen, J., & David, L. 2015, A&A, 575, A30
Sijacki, D., Pfrommer, C., Springel, V., et al. 2008, MNRAS, 387, 1403
Sijacki, D., & Springel, V. 2007, Heating Versus Cooling in Galaxies and Clusters of Galaxies (Berlin: Springer), 237
Simionescu, A., Allen, S. W., Mantz, A., et al. 2011, Sci, 331, 1576
Simionescu, A., Werner, N., Mantz, A., et al. 2017, MNRAS, 469, 1476
Simionescu, A., Werner, N., Urban, O., et al. 2013, ApJ, 775, 4
Snowden, S. L., Mushotzky, R. F., Kuntz, K. D., et al. 2008, A&A, 478, 615
Springel, V., Pakmor, R., Pillepich, A., et al. 2018, MNRAS, 475, 676
Su, Y., Buote, D., Gastaldello, F., & Brighenti, F. 2015, ApJ, 805, 104
Su, Y., White, R. E., & Miller, E. D. 2013, ApJ, 775, 89
Sugizaki, M., Kamae, T., & Maeda, Y. 2009, PASJ, 61, S55
Szydłowski, M., Krawiec, A., Kurek, A., et al. 2015, EPJC, 75, 5
Tchernin, C., Eckert, D., Ettori, S., et al. 2016, A&A, 595, A42
Thölken, S., Lovisari, L., Reiprich, T. H., et al. 2016, A&A, 592, A37
Tozzi, P., & Norman, C. 2001, ApJ, 546, 63
Trotta, R. 2017, arXiv:1701.01467
Truong, N., Rasia, E., Mazzotta, P., et al. 2018, MNRAS, 474, 4089
Urban, O., Simionescu, A., Werner, N., et al. 2014, MNRAS, 437, 3939
van der Vaart, A. W. 1998, Asymptotic Statistics (Cambridge: Cambridge Univ. Press)
Vazza, F. 2011, MNRAS, 410, 461
Vazza, F., Eckert, D., Simionescu, A., Brüggen, M., & Ettori, S. 2013, MNRAS, 429, 799
Vikhlinin, A., Kravtsov, A., Forman, W., et al. 2006, ApJ, 640, 691
Vikhlinin, A., Markevitch, M., Murray, S. S., et al. 2005, ApJ, 628, 655
Voit, G. M., Balogh, M. L., Bower, R. G., et al. 2003, ApJ, 593, 272
Voit, G. M., Bryan, G. L., Balogh, M. L., & Bower, R. G. 2002, ApJ, 576, 601
Voit, G. M., Kay, S. T., & Bryan, G. L. 2005, MNRAS, 364, 909
Walker, S. A., Fabian, A. C., Sanders, J. S., et al. 2013, MNRAS, 432, 554
Walker, S. A., Fabian, A. C., Sanders, J. S., & George, M. R. 2012a, MNRAS, 427, L45
Walker, S. A., Fabian, A. C., Sanders, J. S., & George, M. R. 2012b, MNRAS, 424, 1826
Walker, S. A., Fabian, A. C., Sanders, J. S., George, M. R., & Tawara, Y. 2012c, MNRAS, 422, 3503
Wong, K.-W., & Sarazin, C. L. 2009, ApJ, 707, 1141
Zhang, Y.-Y., Böhringer, H., Finoguenov, A., et al. 2006, A&A, 456, 55
Zhu, Z., Xu, H., Wang, J., et al. 2016, ApJ, 816, 54
Zhuravleva, I., Churazov, E., Arévalo, P., et al. 2015, MNRAS, 450, 4184